

# Modeling and Analysis of Sediment Trapping Efficiency of Large Dams using Remote Sensing

Moragoda Nishani<sup>1</sup>, Cohen Sagy<sup>2</sup>, Gardner John R<sup>3</sup>, Muñoz David<sup>4</sup>, Narayanan Anuska<sup>1</sup>, Moftakhari Hamed R<sup>1</sup>, and Pavelsky Tamlin M<sup>5</sup>

<sup>1</sup>The University of Alabama

<sup>2</sup>University of Alabama, Tuscaloosa

<sup>3</sup>University of Pittsburgh

<sup>4</sup>University of Alabama

<sup>5</sup>University of North Carolina at Chapel Hill

November 16, 2022

## Abstract

Sediment trapping behind dams is currently a major source of bias in large-scale hydro-geomorphic models, hindering robust analyses of anthropogenic influences on sediment fluxes in freshwater and coastal systems. This study focuses on developing a new reservoir trapping efficiency ( $Te$ ) parameter to account for the impacts of dams in hydrological models. This goal was achieved by harnessing a novel remote sensing data product which offers high-resolution and spatially continuous maps of suspended sediment concentration across the Contiguous United States (CONUS). Validation of remote sensing-derived surface sediment fluxes against USGS depth-averaged sediment fluxes showed that this remote sensing dataset can be used to calculate  $Te$  with high accuracy ( $R^2 = 0.98$ ).  $Te$  calculated for 116 dams across the CONUS, using upstream and downstream sediment fluxes from their reservoirs, range from 0.3% to 98% with a mean of 43%. Contrary to the previous understanding that large reservoirs have larger  $Te$  and vice versa, these data reveal that large reservoirs can have a wide range of  $Te$  values. A suite of 21 explanatory variables were used to develop an empirical  $Te$  model using multiple regression. The strongest model predicts  $Te$  using five variables: dam height, incoming sediment flux, outgoing water discharge, reservoir length, and Aridity Index. A global model was also developed using explanatory variables obtained from a global dam database to conduct a global-scale analysis of  $Te$ . These CONUS- and global-scale  $Te$  models can be integrated into hydro-geomorphic models to more accurately predict river sediment transport by representing sediment trapping in reservoirs.

1 **Modeling and Analysis of Sediment Trapping Efficiency of Large Dams using**  
2 **Remote Sensing**

3  
4  
5 \*Nishani Moragoda<sup>1</sup>, Sagy Cohen<sup>1</sup>, John Gardner<sup>2</sup>, David Muñoz<sup>3,4</sup>, Anuska Narayanan<sup>1</sup>, Hamed  
6 Moftakhari<sup>3,4</sup>, Tamlin M. Pavelsky<sup>5</sup>

7  
8 <sup>1</sup>Department of Geography, University of Alabama, Box 870322, Tuscaloosa, AL 35401, USA.

9 <sup>2</sup>Department of Geology and Environmental Science, University of Pittsburgh, Pittsburgh, PA,  
10 USA.

11 <sup>3</sup> Department of Civil, Construction and Environmental Engineering, University of Alabama,  
12 Box 870205, Tuscaloosa, AL 35401, USA

13 <sup>4</sup> Center for Complex Hydrosystems Research, The University of Alabama, Tuscaloosa, AL  
14 35401, USA

15 <sup>5</sup>Department of Earth, Marine and Environmental Sciences, University of North Carolina, Chapel  
16 Hill, NC 27599

17  
18  
19  
20 \*Corresponding author: [npmoragoda@crimson.ua.edu](mailto:npmoragoda@crimson.ua.edu)

21 **Key points**

22

23 Remote sensing-derived surface river sediment fluxes strongly align with depth-averaged river  
24 sediment fluxes with a simple adjustment factor

25

26 Reservoir sediment trapping efficiency ( $Te$ ) was calculated using remote sensing sediment data  
27 to develop empirical CONUS and global  $Te$  models

28

29 Large reservoirs can have a wide range of  $Te$  values, and reservoir volume (reservoir capacity)  
30 does not necessarily determine  $Te$

31 **Abstract**

32 Sediment trapping behind dams is currently a major source of bias in large-scale hydro-  
33 geomorphic models, hindering robust analyses of anthropogenic influences on sediment fluxes in  
34 freshwater and coastal systems. This study focuses on developing a new reservoir trapping  
35 efficiency (*Te*) parameter to account for the impacts of dams in hydrological models. This goal  
36 was achieved by harnessing a novel remote sensing data product which offers high-resolution  
37 and spatially continuous maps of suspended sediment concentration across the Contiguous  
38 United States (CONUS). Validation of remote sensing-derived surface sediment fluxes against  
39 USGS depth-averaged sediment fluxes showed that this remote sensing dataset can be used to  
40 calculate *Te* with high accuracy ( $R^2 = 0.98$ ). *Te* calculated for 116 dams across the CONUS,  
41 using upstream and downstream sediment fluxes from their reservoirs, range from 0.3% to 98%  
42 with a mean of 43%. Contrary to the previous understanding that large reservoirs have larger *Te*  
43 and vice versa, these data reveal that large reservoirs can have a wide range of *Te* values. A suite  
44 of 21 explanatory variables were used to develop an empirical *Te* model using multiple  
45 regression. The strongest model predicts *Te* using five variables: dam height, incoming sediment  
46 flux, outgoing water discharge, reservoir length, and Aridity Index. A global model was also  
47 developed using explanatory variables obtained from a global dam database to conduct a global-  
48 scale analysis of *Te*. These CONUS- and global-scale *Te* models can be integrated into hydro-  
49 geomorphic models to more accurately predict river sediment transport by representing sediment  
50 trapping in reservoirs.

51

52 **Keywords:** Reservoir trapping efficiency, remote sensing, dams, suspended sediment, global  
53 modeling.

54 **1. Introduction**

55 Global fluvial sediment transport is vulnerable to a variety of stresses from human activities  
56 including land use changes, water diversions, and damming (Best, 2019; Lewis et al., 2013, Lu et  
57 al., 2013). Rivers respond to such stresses in numerous and complex ways, which can lead to  
58 various environmental consequences (Li et al., 2020). The construction of dams and  
59 impoundments for hydropower generation, flood control, irrigation, and water supply is among  
60 the greatest stressors to the connectivity and functionality of rivers (Verstraeten and Poesen,  
61 2000; Vörösmarty et al., 2003; Zarfl et al., 2015). Currently, ~58,000 large dams (heights greater  
62 than 15 m) exist in the world with an additional ~3,700 dams that are either planned or under  
63 construction (Best and Darby, 2020; Mulligan et al., 2020; Syvitski and Kettner, 2011). These  
64 impoundments collectively account for a cumulative storage capacity of ~8300 km<sup>3</sup>, which is  
65 equal to around one-sixth of the total annual river discharge to the world's oceans (Lehner et al.,  
66 2011a; Wada et al., 2016). Apart from retaining a large amount of sediment behind them, dams  
67 alter downstream flow regimes affecting sediment carrying capacities, and trigger bank erosion  
68 and riverbed incision driven by sediment starvation from upstream trapping (Best, 2019; Kondolf  
69 et al., 2014b; Schmidt and Wilcock, 2008; Williams and Wolman, 1984). These alterations also  
70 lead to coarsening of the substrate, changes in channel planform, and reductions in sediment-  
71 associated nutrients in downstream areas which could result in collapsed ecosystem functioning  
72 and impacts on the fisheries industry (Brandt, 2000; Syvitski, 2003; Wohl and Rathburn, 2003).  
73 Construction of dams without assessing their potential consequences has led to degraded  
74 floodplain and coastal settings around the world (Latrubesse et al., 2017). In addition, reservoir  
75 sedimentation which is the most important factor affecting the utility and sustainability of  
76 reservoirs, depends on the trapping efficiency of the dam impoundment (i.e., the proportion of  
77 the incoming sediment load trapped in a reservoir) (Jothiprakash and Vaibhav, 2008). Reservoir  
78 sedimentation is a severe problem around the world, affecting water resources management  
79 (Kondolf et al., 2014a; Tan et al., 2019). Reservoir maintenance costs, flood control capacity,  
80 water treatment and distribution strategies, and water availability for domestic and agricultural  
81 uses can also be affected by the trapping efficiency of the reservoir.

82

83 Dams have caused a major reduction in the sediment loads in many of the world's rivers  
84 (Haddeland et al., 2014; Wei et al., 2021; Wu et al., 2020). The Huang He River in China, that

85 once had the highest river sediment flux in the world, is now experiencing diminished water and  
86 sediment flows reaching the coast, in part due to the numerous small and large dams constructed  
87 throughout its watercourse (Wu et al., 2020). The construction of the Hoover dam caused a large  
88 reduction of sediment flux in the Colorado River from about 125 MT/y to 3 MT/y (Williams and  
89 Wolman, 1984). Another widely cited example is the Aswan High Dam in the Nile River that  
90 reduced a pre-dam sediment load of 100 MT/y to nearly zero, causing a rapid shrink in the Nile  
91 River delta (Chakrapani, 2005; Walling, 2012). It has been estimated that approximately 26%  
92 (25-30%) of the global sediment flux is trapped in large reservoirs (Syvitski and Milliman, 2007,  
93 Syvitski et al., 2005; Syvitski et al., 2022; Vörösmarty et al., 2003).

94 Accurate estimation of reservoir trapping is vital for a variety of applications such as, accurately  
95 predicting river sediment transport, quantifying the global sediment delivery into the ocean,  
96 coastal/marine and deltaic environments, understanding anthropogenic influences on riverine  
97 fluxes, simulating future or theoretical change scenarios, evaluating ecological impacts, and  
98 informing dam operations (Merritt et al., 2003; Cohen et al., 2014; Dunn et al., 2019).

99 Representation of sediment trapping by dams is currently a major source of bias in continental-  
100 and global-scale hydro-geomorphic modeling frameworks (e.g., Cohen et al., 2013). Several  
101 methods have been developed and tested over the years to estimate reservoir trapping efficiency  
102 (e.g., Brown, 1943; Churchill, 1948; Brune, 1953; Chen, 1975; Vörösmarty et al., 2003; Borland,  
103 1971; Heinemann, 1984; Verstraeten and Poesen, 2000). The most widely used and adopted  
104 approach is Brune (1953) method where reservoir capacity to inflow ratio is considered in place  
105 of capacity to watershed ratio as previously suggested by Brown (1943). The Brune method was  
106 developed using 40 normally ponded and 4 other types of reservoirs, whereas the Brown method  
107 was based on data from 15 reservoirs. The Brune method was later modified by USDA-SCS  
108 (1983) to include particle size information. They suggested adjustments for dry reservoirs  
109 depending on sand or fine-textured nature of the sediment (Verstraeten and Poesen, 2000). In  
110 contrast, the Churchill (1948) curve calculates a 'sedimentation index' for the reservoir using  
111 residence time of water and flow velocity. It is applicable for reservoir types such as desilting  
112 and semi-dry which are different from normally ponded reservoirs. The Chen (1975) method  
113 predicts trapping for different particle size classes using flow velocity and particle size data.  
114 Rausch and Heinemann (1975) developed an equation that predicts reservoir trapping using

115 reservoir detention time, peak inflow rate (in place of inflow sediment particle size), storm runoff  
116 volume, sediment yield from storm, reservoir storage capacity, and drainage area. This  
117 regression equation, however, was developed using data from only three reservoirs in the  
118 Missouri River for individual storms and was not recommended for reservoirs with different  
119 characteristics. Verstraeten and Poesen (2000) also agreed that trapping efficiency depends on  
120 the inflow sediment characteristics and the water retention time of the reservoir, which in turn  
121 are controlled by reservoir geometry and runoff characteristics.

122 There are numerous factors that may govern variations in sediment trapping by dams. These may  
123 include local climatic, soil, topographic, and geologic conditions, in addition to characteristics of  
124 the river and dam impoundments. The volume of the reservoir relative to inflowing discharge,  
125 type and properties of the dam and reservoir, and sediment properties have been identified as key  
126 variables that govern sediment trapping in individual reservoirs (Brune, 1953; Heinemann, 1984;  
127 Kummur et al., 2010). For example, channel bed sediment composition may be a determining  
128 factor of sediment trapping owing to its erodibility and availability of fine/coarse sediment in the  
129 watercourse. Particle size of the incoming sediment flow was found to be an influencing factor  
130 that determines trapping efficiencies by many researchers (Rausch and Heinemann, 1975;  
131 Jothiprakash and Vaibhav, 2008). This also depends on the soils in the catchment and erosional  
132 processes (Verstraeten and Poesen, 2000). Larger particle sizes resulting from high intensity  
133 storm events yield high trapping efficiencies and vice versa. Therefore, if fine sediment  
134 dominates the watercourse, that may reduce trapping efficiency of the reservoir (Rausch and  
135 Heinemann, 1975). Regional climatic characteristics are also observed to have an influence on  
136 sediment trapping in reservoirs due to low mean annual flows in arid and semi-arid rivers  
137 compared to humid rivers with the same capacity to inflow ratio (Brune, 1953). Rausch and  
138 Heinemann (1975) suggested that factors such as reservoir capacity below the lowest spillway  
139 intake, length of reservoir, and depth through which particles must settle to be trapped may also  
140 affect trapping efficiency. Water retention time of the reservoir also depends on geometric  
141 characteristics of the reservoir such as storage capacity, shape, surface area, and outlet and  
142 spillway location (Jothiprakash and Vaibhav, 2008). In addition, runoff and discharge  
143 characteristics can affect trapping (Verstraeten and Poesen, 2000). Therefore, developing

144 accurate empirical models for estimating reservoir trapping efficiencies requires a  
145 comprehensive evaluation of globally available parameters such as those mentioned above.

146 Many large-scale sediment transport models currently rely on the approach of Vörösmarty et al.  
147 (2003) to calculate trapping as a function of local residence time change, an approximation of the  
148 Brune (1953) method. This method is convenient to use in large-scale models due to its  
149 simplicity and low input data requirement. These simplifications, however, can lead to increased  
150 bias and uncertainty. In addition, these methods have been developed using a limited number of  
151 dams in selected regions, and therefore, may not apply to reservoirs with different flow regimes  
152 and sediment production (Verstraeten and Poesen, 2000). There are a few reported instances  
153 where these methods significantly overestimated or underestimated trapping efficiency in  
154 reservoirs (e.g., Espinosa-Villegas and Schnoor, 2009; Lewis et al., 2013), however, to our  
155 knowledge, no large-scale comparison between measured and estimated sediment trapping  
156 efficiencies in individual reservoirs and dams have been reported in the literature. In order to  
157 calculate trapping efficiency using in situ measurements, long-term observations of sediment  
158 fluxes both upstream and downstream of a reservoir are needed, which are extremely rare.

159 Monitoring of river sediment loads by traditional field methods only provides point  
160 measurements at the gaging station and has limited spatial and temporal coverage (Cohen et al.,  
161 2013; Fagundes et al., 2020). These methods are also costly to establish and maintain and  
162 therefore, ongoing sediment monitoring programs worldwide are increasingly being terminated  
163 (Syvitski et al., 2005). Gaging stations for calculating sediment trapping are typically located far  
164 upstream and/or downstream of dams, which can introduce considerable errors to the trapping  
165 efficiency calculations (Brune, 1953). Given these limitations, traditional field methods do not  
166 provide sufficient data points to calculate incoming and outgoing sediment at reservoirs nor  
167 continuous data to construct longitudinal sediment profiles along rivers at large spatial scales.  
168 Numerical methods are increasingly being developed to simulate spatially and temporally  
169 distributed sediment dynamics in fluvial systems, however, providing accurate estimates of  
170 sediment loads still remains challenging due to our limited knowledge of the numerous  
171 interconnected processes that govern sediment dynamics and the difficulties in representing these  
172 complexities in models (Pelletier et al., 2012; Vercruyssen et al., 2017). Sediment or turbidity  
173 rating curves are another option to obtain sediment data upstream and downstream of reservoirs,

174 but the relationship between discharge and sediment/turbidity is highly complex and varies in  
175 both time and space, and therefore prone to errors (Wang et al., 2021a).

176 Emerging remote sensing methodologies and datasets of fluvial sediment (Dethier et al., 2020;  
177 Gardner et al., 2021; Overeem et al., 2017; Yang et al., 2022) provide a unique opportunity to  
178 quantify, analyze, and model sediment trapping and its downstream impacts at continental and  
179 global scales. Remote sensing can also provide temporal dynamics, which is important as  
180 sediment trapping and its downstream impacts can vary over time (Rausch and Heinemann,  
181 1975). Longitudinal sediment profiles developed using remote sensing data also provide  
182 opportunities to study spatial and temporal recovery patterns of the river system downstream of a  
183 dam.

184  
185 This paper is focused on the development of conceptual understanding and parameterization of  
186 sediment trapping efficiency of large dams and exploring sediment dynamics downstream of  
187 dams. A novel reservoir trapping efficiency empirical model is developed using a new remote  
188 sensing dataset (Gardner et al., 2022) that offers high-resolution and spatially continuous  
189 suspended sediment concentration (SSC) data across the Contiguous United States (CONUS) for  
190 1984-2018. This is the first dataset of its kind that enables the observation and modeling of  
191 fluvial suspended sediment dynamics at a continental scale, a transformative capability  
192 considering the scarcity in sediment gaging. Suspended sediment loads upstream of a reservoir  
193 and downstream of its dam are used to calculate sediment trapping in 116 reservoirs. These  
194 reservoir trapping data are used to develop a new reservoir trapping efficiency empirical model  
195 using widely available fluvial, environmental, and dam attributes. This analysis provides insights  
196 into the factors controlling the magnitude of suspended sediment trapping by dams at large  
197 spatial scales. In order to develop these quantitative relations, we employ statistical approaches  
198 such as multiple regression as well as machine learning techniques. We developed an additional  
199 model based on a global dataset of dams to extend our estimation of sediment trapping globally,  
200 providing a unique attribute for future analyses and modeling efforts. We also discuss the  
201 changes in suspended sediment loads downstream of dams using longitudinal sediment profiles  
202 extracted from the remote sensing dataset.

203 **2. Methods**

204 **2.1. Dam selection and trapping efficiency calculation**

205 The remote sensing sediment dataset used in this study was developed by Gardner et al. (2022),  
206 using Landsat 5, 7, and 8 processed in Google Earth Engine (GEE) and Machine Learning to  
207 convert imagery to SSC, generating high-resolution and spatially continuous maps of long-term  
208 averaged (1984-2018) SSC across the CONUS. This approach provides SSC (mg/L) data linked  
209 to the National Hydrography Dataset (NHDplus V21) river network (McKay et al., 2015). For  
210 more information about this data product and its validation, readers are referred to Gardner et al.  
211 (2021) and Gardner et al. (2022).

212  
213 For this study, we calculated long-term averaged suspended sediment flux (kg/s) for each  
214 NHDPlus river reach by multiplying its remote sensing-derived SSC (mg/L) and NHDplus mean  
215 annual discharge ( $\text{m}^3/\text{s}$ ). We used suspended sediment flux to calculate trapping efficiency  
216 instead of SSC to mitigate issues of water extraction and loss in reservoirs due to irrigation and  
217 evaporation, which can skew the calculation. For example, low sediment loads can be indicated  
218 as high sediment concentrations if a significant amount of water is extracted and removed from  
219 the system. Therefore, it is important to use flux values when calculating reservoir trapping even  
220 if it introduces an additional source of bias from the NHDplus discharge estimates.

221  
222 We conducted a validation of the calculated suspended sediment flux values, and the NHDplus  
223 discharge values used to calculate them, against USGS gage sediment flux and water discharge  
224 data, respectively. The main objective of the validation was to find how well suspended sediment  
225 flux calculated by remote sensing-derived surface SSC represents the total, depth-integrated  
226 suspended sediment load of the river. The validation was conducted for 36 USGS gage sites  
227 where daily suspended sediment discharge measurements were available over the same period of  
228 time, and for sites located on the river network for which remote sensing data were available  
229 (Supplementary Table S1). However, the temporally-averaged USGS sediment flux values for  
230 some gaging stations do not represent the entire period of the remote sensing data. Based on this  
231 validation of suspended sediment flux, we introduced a simple adjustment factor to match the  
232 remote sensing-calculated surface suspended sediment fluxes to depth-averaged suspended  
233 sediment fluxes.

234

235 For the CONUS-scale analysis, we used the National Inventory of Dams (NID) dataset,  
236 published by the U.S. Army Corps of Engineers (<https://nid.sec.usace.army.mil/ords/>). The NID  
237 consists of more than 91,000 dams with attributes such as dam storage, dam height, dam length,  
238 drainage area, surface area of the impoundment, dam history, inspection, and hazard potential.  
239 We conducted an initial filtering to extract the dams located on the river network for which  
240 remote sensing sediment data were available, and have valid (non-zero) values for reservoir  
241 storage, drainage area, dam height, and dam length. Then through a meticulous manual  
242 procedure involving ArcGIS base maps, Google Earth, USA detailed water bodies layer package  
243 (ESRI, 2021), Global Reservoir and Dam (GRanD) Database (Lehner et al., 2011b), and  
244 NHDWaterbody layer, the locations of dams and reservoirs that correspond to the river network  
245 with remote sensing data were extracted. This resulted in 412 dams in total that are distributed  
246 across the CONUS. 189 cascading dams (where the next dam impoundment starts immediately  
247 or closely after the upstream dam) were removed from trapping efficiency calculations.  
248 However, we propose that cascading dams need to be further explored in the future to understand  
249 their role in sediment trapping and develop better models for predicting their  $Te$ . In this study, it  
250 was not realistic to calculate  $Te$  for cascading dams using remote sensing data as the incoming  
251 and outgoing river reach features for cascading dam impoundments mostly fall within the  
252 reservoir polygons.

253

254 Sediment trapping efficiency ( $Te$ ; %) for individual dams was calculated as:

255

$$256 \quad Te = \frac{Q_{s\_in} - Q_{s\_out}}{Q_{s\_in}} * 100 \quad (1)$$

257

258 where,  $Q_{s\_in}$  is the suspended sediment flux entering the reservoir (kg/s), and  $Q_{s\_out}$  is the  
259 suspended sediment flux immediately downstream of the dam. If there are multiple river reaches  
260 entering the reservoir,  $Q_{s\_in}$  is equal to the sum of suspended sediment flux from all these  
261 reaches depending on data availability. For most of the dams, however, remotely sensed  
262 suspended sediment data were not available for all river reaches entering the reservoir.

263 Therefore, the incoming sediment flux into the reservoir may be underestimated, leading to  
264 conservative (underestimated)  $Te$  values.

265

266 Out of the 412 dams, 105 yielded negative  $Te$  values because outgoing sediment fluxes were  
267 greater than incoming sediment fluxes, indicating that these dams do not trap any sediment. The  
268 reasons for a negative  $Te$  may include (i) remotely sensed data capture the channel/bank erosion  
269 that occurs immediately after the dam, (ii) large tributaries that join the reservoir or the river  
270 reach immediately after the dam bring large amounts of sediment, (iii) lack of remote sensing  
271 sediment data for some of the incoming river reaches into the reservoir, (iv) dams use  
272 mechanisms to release sediment downstream, (v) bias in remote sensing sediment data, and (vi)  
273 in a few instances, the NHDplus river reach feature upstream of the reservoir, or downstream of  
274 the dam captures a part of the reservoir.

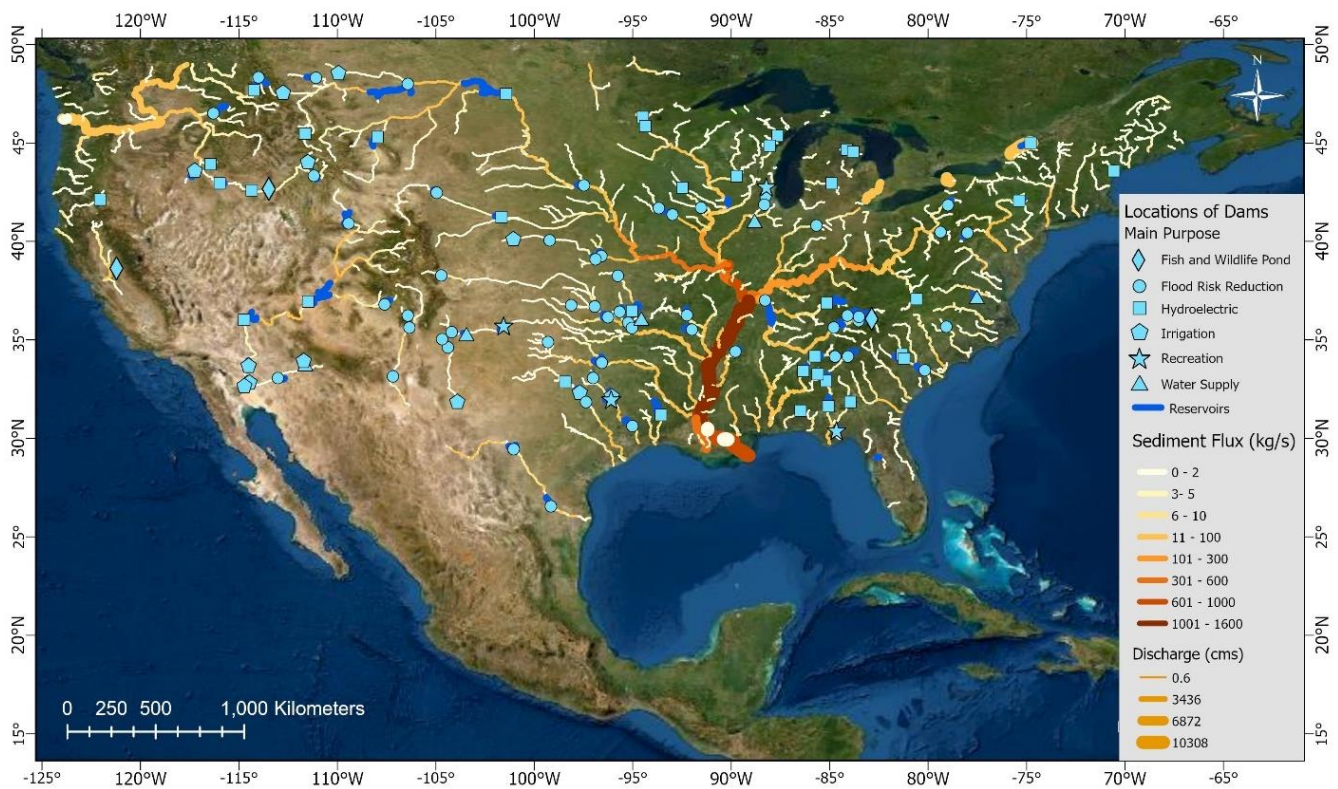
275

276 Further investigation into the 105 dams that yielded negative  $Te$  values (indicating no sediment  
277 trapping) revealed that the main purpose of the dam may play a role in determining sediment  
278 trapping. Many dams with negative  $Te$  values in our dataset belong to those with a primary  
279 purpose of navigation and hydropower generation. Out of the 30 dams that had navigation  
280 designated as their primary use, 28 indicated no sediment trapping, whereas out of the 80 dams  
281 that had hydroelectricity designated as their primary use, 37 indicated no sediment trapping. On  
282 the contrary, dams built with the main purpose of irrigation, water supply, or flood risk reduction  
283 had only a few dams with zero  $Te$  values. However, it should be noted that many of these dams  
284 have multiple uses. This observation is reasonable as navigational dams or lock and dam  
285 structures are usually designed to release water, and thus sediment, downstream. Dams built for  
286 hydroelectricity, particularly run-of-river hydroelectric dams have little or no water storage and  
287 thus natural seasonal river flows are less obstructed. In contrast, dams and reservoirs built for  
288 water use purposes such as irrigation and water supply need to store the water. Taking this  
289 distinction into consideration, all dams with 'navigation' designated as their primary purpose  
290 were considered as having zero  $Te$ . However, no information was available in the NID dataset to  
291 distinguish run-of-river hydroelectric dams from conventional hydropower dams with  
292 impoundments. Therefore, all the hydropower dams with positive  $Te$  values were included in the

293 dataset. After removing cascading dams, dams with a negative  $Te$ , and navigational dams, 116  
294 dams were available for use in the analysis (Figure 1).

295

296 A potential problem associated with calculating  $Te$  using remotely sensed upstream and  
297 downstream sediment loads is that  $Q_{s\_out}$  captures the erosion taking place in downstream  
298 reaches. Therefore, the amount of sediment trapped may be higher than the calculated  $Te$ . This  
299 is, however, also an issue for calculating trapping using gage data from upstream and  
300 downstream of the reservoir, which is the standard method to calculate observed trapping  
301 efficiencies of dams.



302 **Figure 1:** Map of the locations of 116 dams and reservoirs used in the analysis along with the river  
303 sediment fluxes calculated using the remote sensing data.

304

## 305 2.2. CONUS $Te$ Model Development

306 Several environmental, fluvial, and dam-related variables that are widely available were  
307 collected to develop a CONUS-wide empirical  $Te$  model (Table 1). In addition to dam attributes  
308 provided by the NID dataset, we extracted fluvial, environmental, and dam attributes from the  
309 following geospatial datasets: NHDplus river network, Global River Width Dataset (Lin et al.,

2020), Reservoir Morphology Database for the Conterminous United States (Rodgers, 2017), Free Flowing Rivers dataset (FFR; Grill et al., 2019), GRanD database (Lehner et al., 2011b), GLObal geOreferenced Database of Dams (GOODD; Mulligan et al., 2020), and GeoDAR global reservoir and dam dataset (Wang et al., 2021b) with attributes acquired from the World Register of Dams (WRD) maintained by the International Commission on Large Dams (ICOLD; <https://www.icold-cigb.org>). Reservoir length along its longest part was calculated along the NHDplus river network using reservoir polygons. The relationship between these variables and  $Te$  was analyzed using multiple regression and machine learning. We used machine learning techniques, such as Random Forest Regression and Artificial Neural Network (e.g., Multi-layer Perceptron) models, with an 80% and 20% split of data for training and validation, respectively. Sensitivity and variable selection analyses (e.g., Variance Inflation Factor) were conducted to identify the key attributes that contain the largest variance of the data. In addition, we also applied Geographically Weighted Regression (GWR) to the dataset to identify local spatial variations in the relationship between explanatory variables and  $Te$ .

**Table 1:** Explanatory variables tested for developing the  $Te$  parameter

Variable	Symbols	Data type	Data source*
Incoming sediment flux	$Qs_{in}$	Line	Gardner et al. (2022)
Incoming discharge	$Q_{in}$	Line	NHDplus V21
Outgoing discharge	$Q_{out}$	Line (NHDplus), point (GRanD)	NHDplus V21, GRanD
Dam length	$D_{Length}$	Point	NID, GRanD
Dam height	$H$	Point	NID, GRanD
Reservoir storage	$S$	Point	NID, GRanD
Reservoir surface area	$SA$	Point	NID, GRanD
Drainage area	$D$	Point	NID, GRanD
Slope	$Slp$	Line	Lin et al. (2020)
Elevation	$Elev$	Line (Lin), point (GRanD)	Lin et al. (2020), GRanD
% Sand	$Snd$	Line	Lin et al. (2020)
% Silt	$Slf$	Line	Lin et al. (2020)
% Clay	$Cly$	Line	Lin et al. (2020)
Sinuosity	$Sin$	Line	Lin et al. (2020)
Aridity Index	$AI$	Raster (~1 km)	Lin et al. (2020), Trabucco and Zomer (2019)
Leaf Area Index	$LAI$	Line	Lin et al. (2020)

Sum of soil erosion from within the river reach catchment	$E$	Line	Grill et al. (2019)
2-yr return period flood	$Q2$	Line	Lin et al. (2020)
Dam age	$A$	Point	NID, GRanD
Lake length	$L$	Line	Grill et al. (2019)
Reservoir Depth	$Depth$	Point	GRanD

325

### 326 **2.3. Calculation and Analysis of a Global $T_e$ Dataset**

327 To enable a global-scale analysis, we also developed a global empirical  $T_e$  model using dam  
328 attributes from the GRanD database (Lehner et al., 2011b). In addition to the observed  $T_e$  values  
329 for the 116 US dams, observed  $T_e$  was calculated for 4 dams in the Amazon Basin using a  
330 similar remote sensing dataset (Narayanan, 2022). Observed  $T_e$  for 36 dams in China (Hu et al.,  
331 2009; Tan et al., 2019), the Bhakra Dam in India (Jothiprakash and Vaibhav, 2008; Sharma et al.,  
332 2018), and the Aswan High Dam in Egypt (Biswas and Tortajada, 2012) were derived from the  
333 literature. Thus, a total of 158 observed  $T_e$  values were used to develop this global  $T_e$  model.  
334 Some of the missing explanatory variable data for these 158 dams in GRanD were substituted  
335 with data from the NID dataset, or the GeoDAR global reservoir and dam dataset (Wang et al.,  
336 2021b) with attributes acquired from the World Register of Dams (WRD). We then applied the  
337 global  $T_e$  model to the entire GRanD dataset to conduct global- and continental-scale analyses.  
338 Some of the missing dam height data in GRanD were substituted using the GeoDAR dataset and  
339 ICOLD attributes. For this global-scale application, reservoir lengths were calculated using an  
340 automated process involving the Grill et al. (2019) river network and GRanD reservoir polygons.  
341 GRanD dams that had missing data for essential explanatory variables, and dam impoundments  
342 that did not fall on the Grill et al. (2019) river network were excluded from the analysis, which  
343 resulted in 6823 dams for this analysis. The GRanD dataset does not include a reservoir polygon  
344 for individual dams such as barrages, diversions, or run-of-the-river hydropower stations, which  
345 may not form reservoirs. For these dams, and dams with navigation designated as the main use in  
346 the GRanD database, the  $T_e$  was assigned as zero. This dataset is envisioned to provide a  $T_e$   
347 parameter for large-scale hydrological and geomorphic modeling frameworks.

348 **3. Results and Discussion**

349 **3.1. Evaluation of the Remote Sensing Sediment Data**

350 A major limitation of remote sensing of sediment is that it can only capture sediment  
351 concentration for the top layer of the river water column. Existing theoretical methods to obtain  
352 depth-averaged sediment concentration profiles such as the Rouse profile require data on water  
353 depth, sediment settling velocity, shear velocity at different water depths, and other coefficients  
354 (Laguionie et al., 2007) which are not readily available. Blanchard et al. (2011) reported that  
355 suspended sediment concentration varied at different depths among different sites they measured.  
356 A universal method to estimate sediment concentration profiles using surface sediment fluxes  
357 has yet to be developed. We conducted a comparison between USGS measured and remote  
358 sensing-calculated sediment fluxes for 36 gaging stations. The results show that the remote  
359 sensing sediment flux is consistently underestimated (Figure 2b).

360

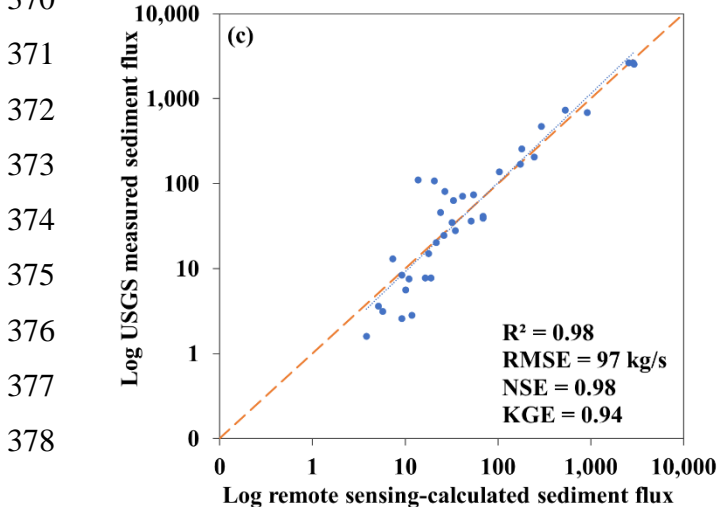
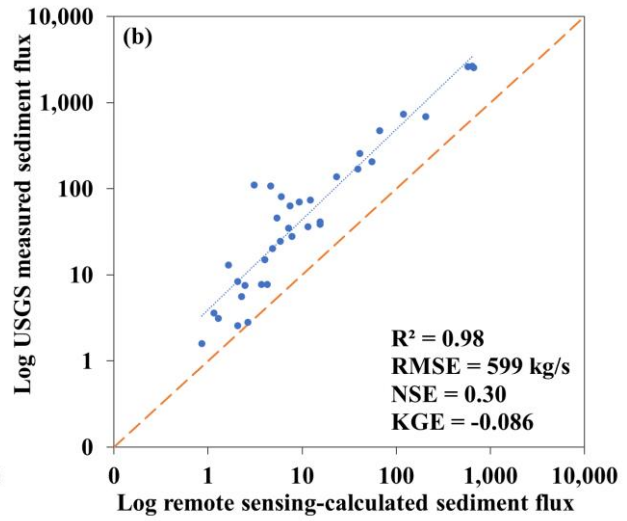
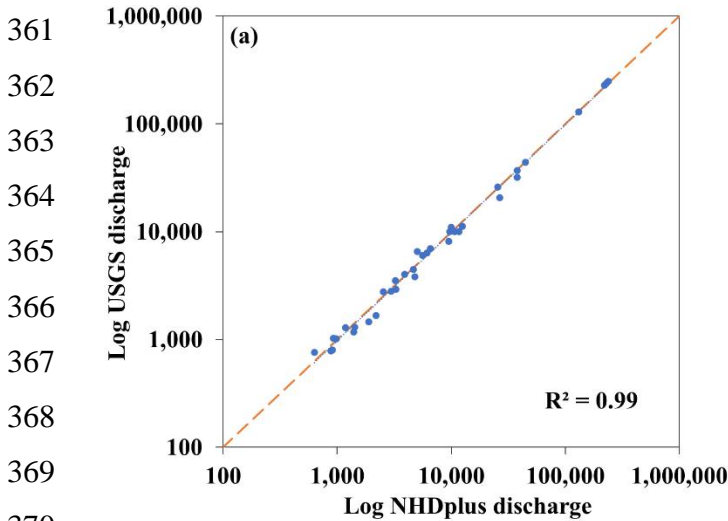


**Figure 2:** Comparison of (a) NHDplus discharge with USGS measured discharge ( $R^2 = 0.99$ ), (b) suspended sediment flux calculated using remote sensing data (and NHDplus discharge) with suspended sediment flux measured at USGS gage stations ( $R^2 = 0.98$ ), and (c) suspended sediment flux calculated using remote sensing data (and NHDplus discharge) with USGS measured suspended sediment flux, after incorporating the adjustment factor of 4.454436 ( $R^2 = 0.98$ ).  $n=36$  for all graphs.  $R^2$  = Coefficient of Determination, RMSE = Root Mean Square Error, NSE = Nash Sutcliffe Efficiency, KGE = Kling Gupta Efficiency.

379

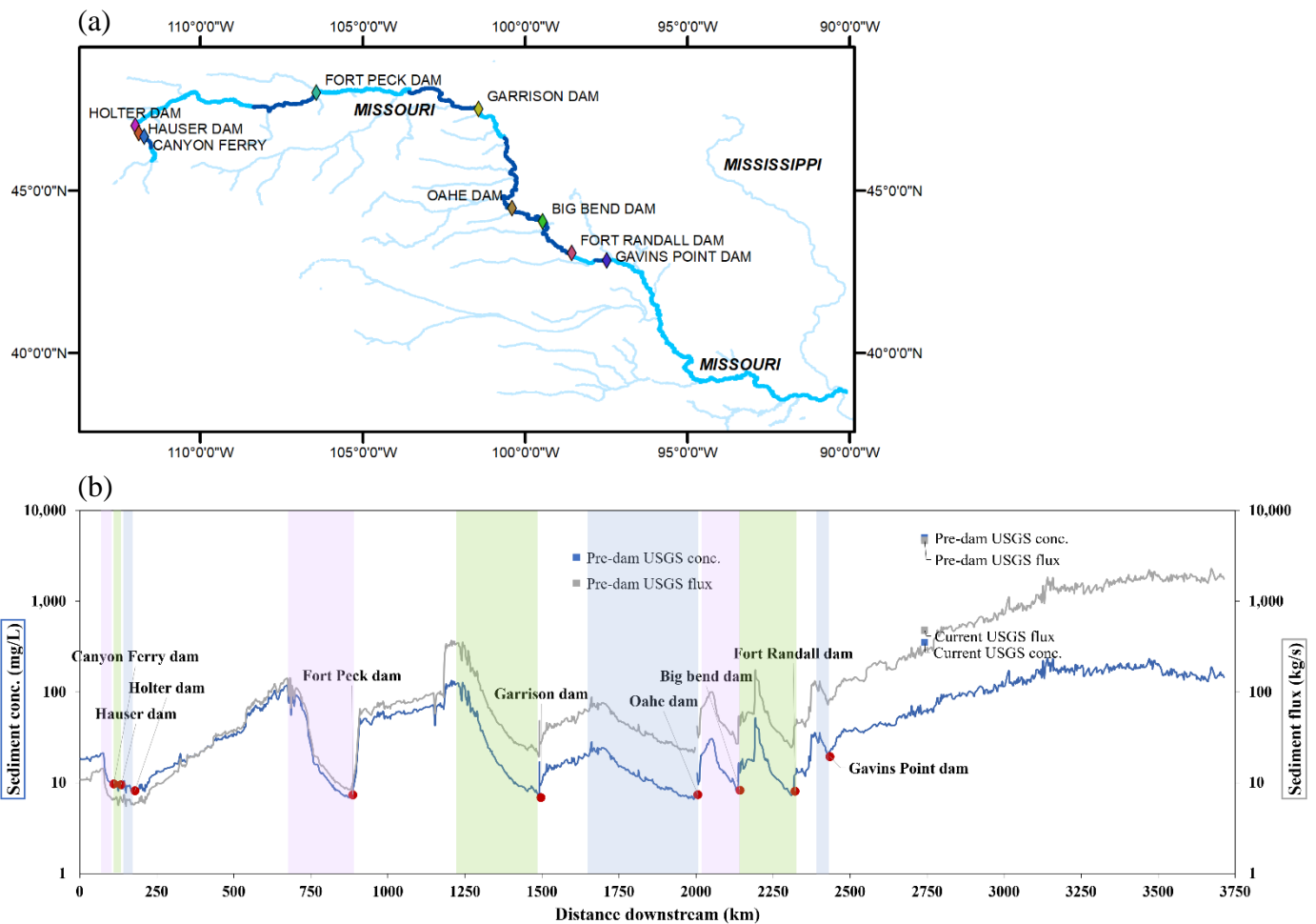
380 A comparison between NHDplus discharge and USGS measured discharge shows that the  
381 discharge values correspond nearly perfectly to the in-situ measurements and, hence are highly  
382 reliable (Figure 2a). This may also be attributed to the fact that NHDplus mean annual discharge  
383 is gage adjusted based on the observed flow (Moore et al., 2019). NHDplus is, however, widely  
384 used in hydrological studies as a reliable source of mean annual discharge, so we are quite  
385 confident in these values throughout the CONUS. We can therefore conclude that the source of  
386 underestimation of the calculated sediment flux is that it reflects water surface suspended  
387 sediment concentration. A simple adjustment factor of 4.45 yields the strongest alignment with  
388 the 1:1 line, yielding the lowest sum of residuals and improved model performance statistics  
389 (RMSE, NSE, and KGE), so that sediment flux calculations are representative of the depth-  
390 averaged sediment flux in the in-situ observations (Figure 2c). This result shows that remote  
391 sensing-derived suspended sediment fluxes can be used to calculate  $Te$  with high accuracy using  
392 a simple adjustment factor. The efficiency of the uniform adjustment factor is surprising given  
393 the diversity of the gage locations, the range of sediment flux values (3 orders of magnitude), and  
394 the known complexity in the fluvial sediment-depth relationship. The strong linear fit in figure  
395 2c implies that average surface suspended sediment flux is uniformly 4.45 times smaller than  
396 depth-averaged flux across a wide range of rivers over the CONUS. This finding merits further  
397 investigation using a wider geographical range. A smarter adjustment factor may be warranted to  
398 reduce the relatively high scatter observed for smaller values of sediment flux, though, more data  
399 would be required to develop such an adjustment factor.

400

### 401 **3.2. Sediment Dynamics Along Longitudinal Profiles**

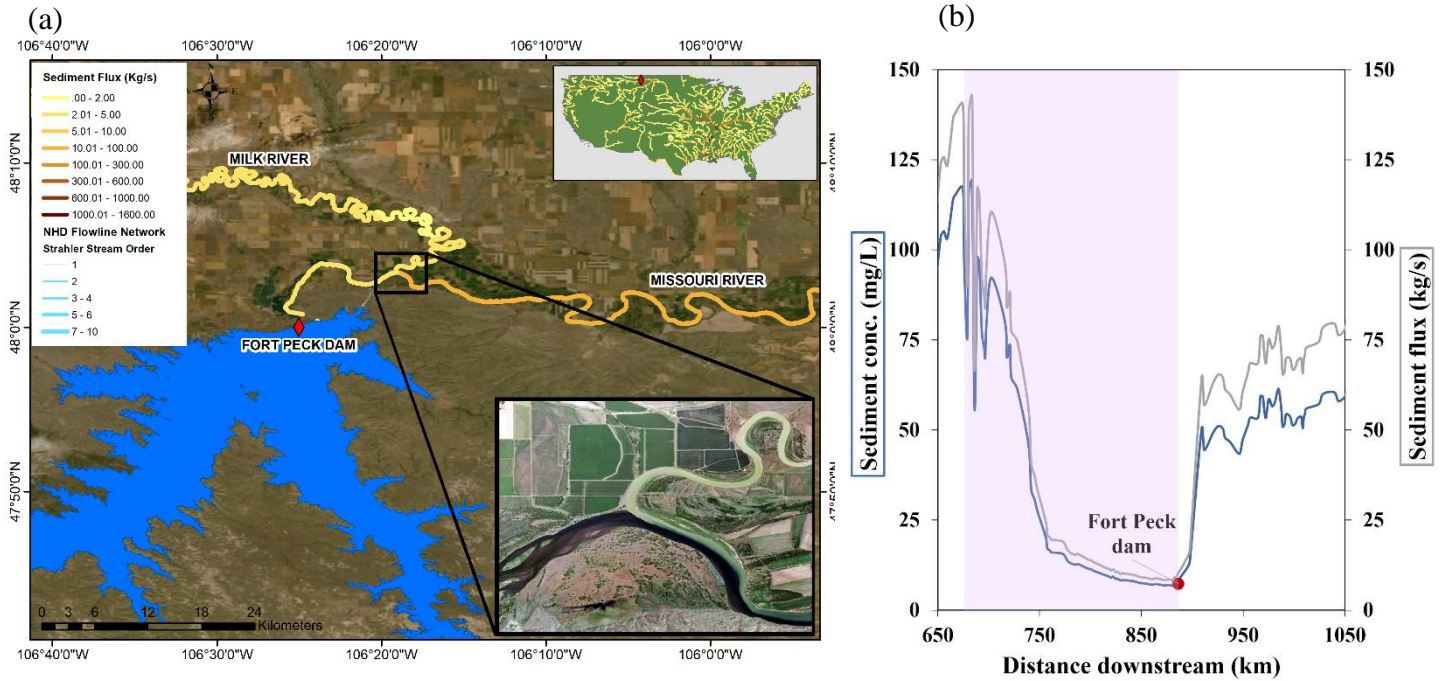
402 The Missouri River is a great case study to examine the changes in sediment dynamics along its  
403 longitudinal profile due to obstruction by a diverse set of large dams (Figure 3). The largest of  
404 these dams in terms of reservoir capacity include the Garrison Dam forming Lake Sakakawea,  
405 Oahe Lake and Dam, and Fort Peck Lake and Dam, with reservoir storage capacities of 32.1  
406 km<sup>3</sup>, 29.1 km<sup>3</sup>, and 23.6 km<sup>3</sup>, respectively. As expected, both the sediment concentration and  
407 flux generally increase as the river flows downstream. The trends in sediment concentration and  
408 flux are generally similar. A rapid decrease in the sediment load (both concentration and flux) is  
409 observed within reservoirs (highlighted color sections in Figure 3b). This shows the deposition of

410 sediment in the reservoir due to reduced flow velocity (Verstraeten and Poesen, 2000). Near the  
 411 headwaters of the Missouri River, sediment flux increases downstream at a rate of 0.05 kg/s/km,  
 412 and then a steep decrease in sediment is observed once it reaches the first set of relatively small  
 413 cascading dams (collectively account for 3.1 km<sup>3</sup> storage capacity). The sediment load increases  
 414 without obstructions from large dams for about 493 km downstream at a rate of 0.27 kg/s/km.  
 415 Once the river enters Fort Peck Lake, sediment load rapidly decreases at a rate of -0.52 kg/s/km  
 416 due to deposition in the reservoir. Fort Peck Dam traps 93.6% of its incoming sediment flux as  
 417 calculated by the remote sensing dataset. Sediment loads increase rapidly immediately after the  
 418 Fort Peck dam due to the high sediment-yielding Milk River confluence (Figure 4).



419 **Figure 3:** Longitudinal profile of sediment dynamics in the Missouri river. (a) Map of the Missouri River  
 420 and its dams. (b) Trend in sediment concentration and flux along the Missouri River. The red dots show  
 421 the dam locations, whereas the blue and grey lines show the sediment concentration (mg/L) and adjusted

422 sediment flux (kg/s) obtained from the remote sensing data, respectively. Pre-dam construction and  
 423 current observed long-term average sediment concentrations (blue squares) and fluxes (grey squares)  
 424 were calculated from USGS gage sites where data are available. The colored areas indicate the extent of  
 425 reservoirs corresponding to the dams. Note that vertical axes are converted to log scale to enhance  
 426 visualization.



427  
 428 **Figure 4:** The Milk River joining the Missouri river immediately after the Fort Peck dam, contributing to  
 429 a sudden increase in downstream sediment load. 5(b) shows the longitudinal sediment profile of the river  
 430 segment with the colored bar showing the reservoir extent. Blue and grey lines show the sediment  
 431 concentration (mg/L) and adjusted sediment flux (kg/s) obtained from the remote sensing data,  
 432 respectively.

433  
 434 The next large dam along the Missouri profile, Garrison (km 1,500 in Figure 3b), traps 85.2% of  
 435 its incoming sediment flux. The pattern of decrease in sediment within the reservoir length and a  
 436 sudden increase in sediment after the dam can also be clearly observed at this location, as well as  
 437 Oahe, Big Bend, and Fort Randall dams and reservoirs. The increase in sediment after the dam at  
 438 Oahe, Big Bend, and Fort Randall dams are gradual increases within a short distance (as opposed  
 439 to the sudden increase after Fort Peck) and can likely be attributed to both instream erosion and  
 440 sediment influx from smaller tributaries. The spike after the Garrison dam could be due to the

441 turbidity at the start of the spillway. The spike in sediment flux and concentration at km 2,192  
442 within Lake Francis Case (formed by the Fort Randall Dam) is due to the White River joining  
443 the Missouri river. The increase in sediment between Fort Randall dam and Lewis and Clark  
444 Lake (formed by Gavins Point dam) at 2,374 km downstream point is due to the Niobrara River  
445 joining the Missouri River. Gavins Point dam also shows a similar pattern of sediment trapping  
446 and a gradual increase downstream. Along its most downstream segment (~2,400 – 3,750 km),  
447 the Missouri River flows without dam obstructions until it joins the Mississippi River, gaining  
448 sediment along the way, with considerable contribution from tributaries. The rate of increase in  
449 sediment flux along this segment of Missouri is 1.32 kg/s/km.

450

451 USGS gage sediment concentration and flux data prior to dam construction were obtained for  
452 two locations along the Missouri River: Missouri River at Bismarck, ND at km 1,612 (USGS  
453 gage number: 06342500) and Missouri River at Omaha, NE at km 2,741 (USGS gage number:  
454 06610000). The latter also provide post dam-construction measurements. For the Bismarck  
455 station, daily sediment data were available only for the year 1946, therefore, this was used to  
456 calculate the average sediment loads prior to dam construction. For the Omaha station, average  
457 prior-to-dam sediment concentration and flux were calculated using daily data for the period  
458 between 1939 – 1951, while current sediment concentration and flux were calculated using daily  
459 data for the period between 1991 – 2019 (excluding 2004 – 2007 due to missing data). The  
460 current sediment flux from USGS data at Omaha station (477 kg/s) compares reasonably well  
461 with the adjusted sediment flux from remote sensing data for this location (294 kg/s),  
462 considering the difference in the temporal range. The difference between the prior-to-dam and  
463 contemporary sediment fluxes observed at the gage site is over an order of magnitude at the  
464 Omaha station (4694 kg/s to 477 kg/s) and two orders of magnitude at the Bismarck station  
465 (1587 kg/s to 49 kg/s).

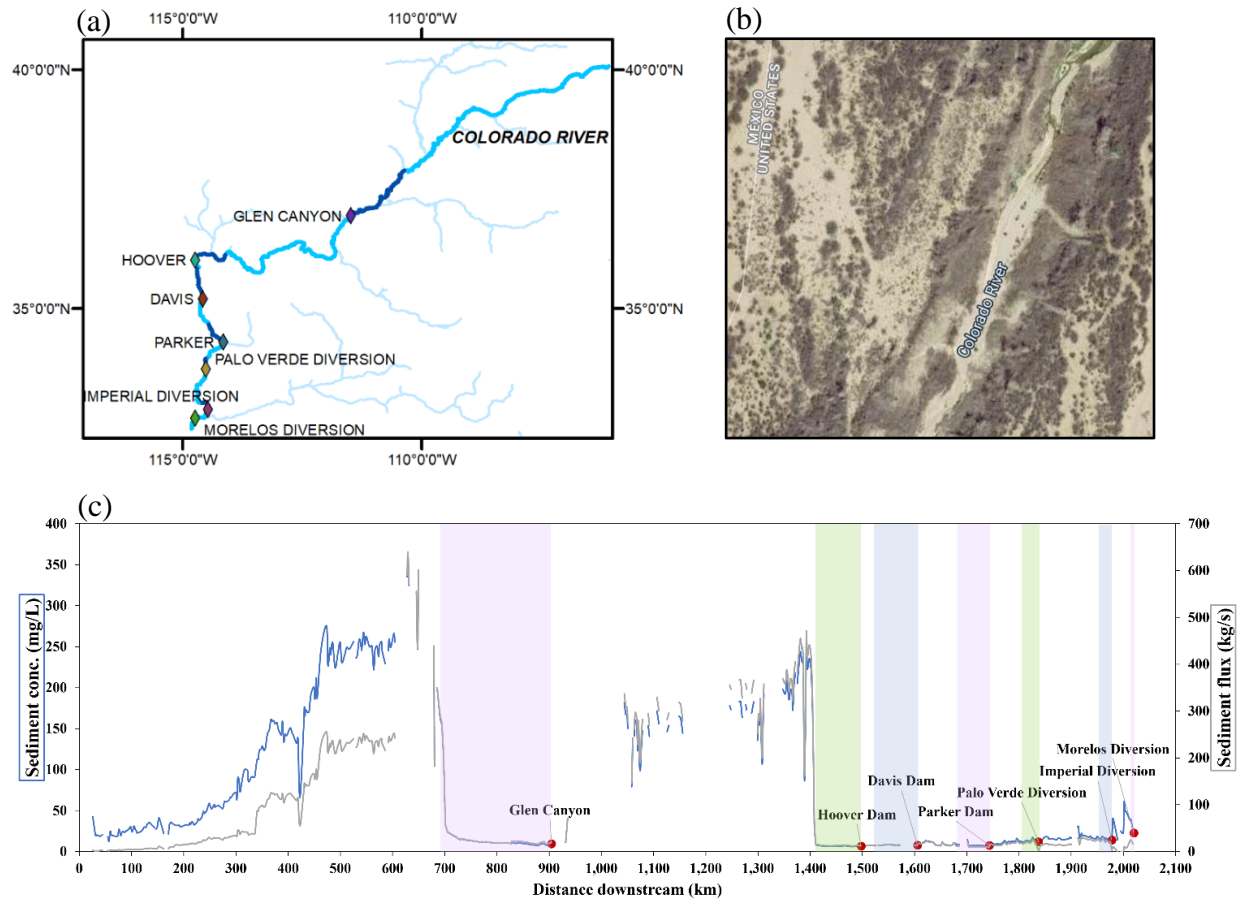
466

467 The Colorado River (Figure 5) is well known for its near-zero sediment flux to the ocean due to  
468 the high degree of sediment trapping by dams and water extractions. Sediment load increases at  
469 an average rate of 1.07 kg/s/km from the headwaters in Rocky Mountains National Park, CO,  
470 until km 620, downstream of which sediment load decrease, before entering the Glen Canyon  
471 reservoir (left-most highlighted section in Figure 5c). Glen Canyon Dam traps on average 95%

472 of the incoming sediment load, resulting in a near-zero load downstream. Until the river enters  
473 Lake Mead (formed by the Hoover Dam), sediment flux generally increases at an average rate of  
474 0.84 kg/s/km. The areas with missing (and highly fluctuating) remote sensing-captured SSC  
475 before the start of Lake Powell (formed by the Glen Canyon Dam), as well as in river reaches  
476 between Glen Canyon dam and Lake Mead, are the portions of the Colorado River that flow  
477 through the Canyonlands National Park, and the Grand Canyon, respectively. These more  
478 confined segments of the river pose challenges for remote sensing techniques due to (1)  
479 generally very narrow river widths, (2) steep canyons creating hill shadows, (3) in areas where  
480 rapids/white water areas are interspersed with slow water flows, rapids may be indicated as high  
481 SSC, and (4) a number of small tributaries along this part of the river that deliver considerable  
482 amount of sediment to the Colorado River potentially contributing to the high variability.

483

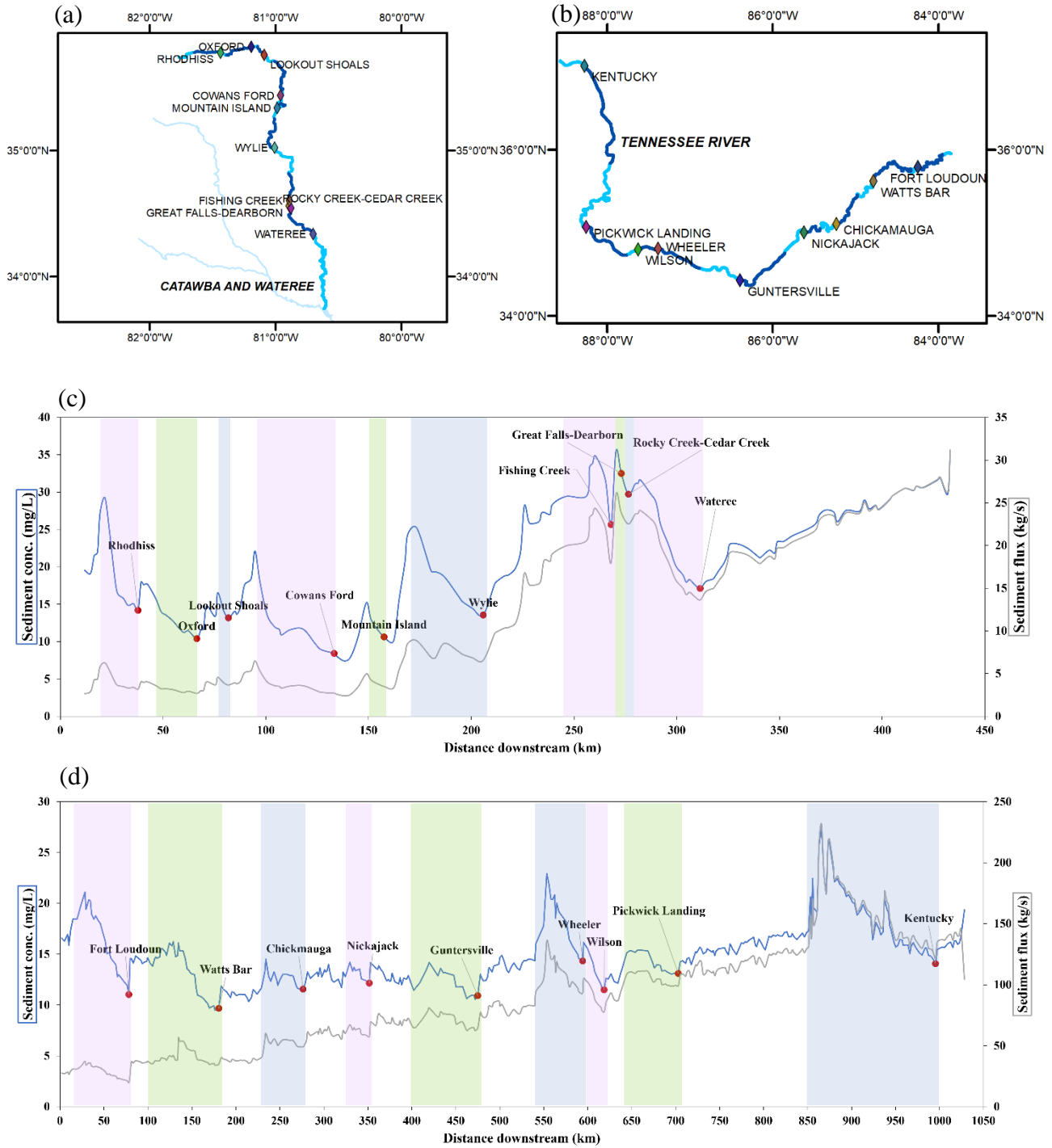
484 The Hoover Dam traps 83.3% of the incoming sediment load, and the dams that follow such as  
485 Davis, Parker, Palo Verde diversion, etc. keep the sediment load from recovering. The Morelos  
486 diversion dam, which is the last dam on the Colorado River, diverts a large portion of its water  
487 for irrigating highly developed croplands in the Mexicali Valley, Mexico. The Colorado River  
488 has a very low water discharge from this point onwards (Figure 5b). Although the NHDplus river  
489 network and therefore sediment data ends at the Morelos diversion dam shortly before reaching  
490 the US-Mexico border, the river extends further until it reaches the ocean. This longitudinal river  
491 profile shows the dynamics leading to a very low sediment flux from the Colorado River to the  
492 ocean.



493  
 494 **Figure 5:** Longitudinal profile of sediment dynamics in the Colorado river. (a) Map of the Colorado  
 495 River and its dams. (b) Colorado River after the Morelos Diversion Dam with very low discharge. (c)  
 496 Mean sediment concentration and flux along the Colorado River. The red dots show the dam locations,  
 497 whereas the blue and grey lines show the sediment concentration (mg/L) and adjusted sediment flux  
 498 (kg/s) obtained from the remote sensing data, respectively. The colored areas indicate the extent of  
 499 reservoirs corresponding to the dams.

500  
 501 Similar patterns in sediment trapping and downstream recovery are observed in other rivers (e.g.,  
 502 Figure 6(c) the Catawba and Wateree Rivers, Figure 6(d) the Tennessee River). In the Catawba  
 503 and Wateree Rivers, clear decreases in sediment concentrations are observed at reservoir  
 504 locations, however, this trend is not very prominent in sediment flux. This may be due to the  
 505 gradual increase in discharge throughout the water course that alleviated the changes in sediment  
 506 concentration until the Wylie dam (km 206). Sediment concentration and flux both increase for  
 507 about 28 km downstream of Wylie dam at a rate of 0.33 kg/s/km until the next set of cascading

508 dams trap a large amount of sediment. Following these dams, a gain in sediment is observed until  
509 the Wateree River and Congaree River confluence, at a rate of 0.14 kg/s/km. In the Tennessee  
510 River (Figure 6d), although sediment concentration shows decreases at reservoir locations,  
511 sediment fluxes show a general increasing trend until the Kentucky Lake (km 846), despite  
512 multiple dam obstructions. Kentucky Dam shows a reduction in both sediment concentration and  
513 flux within the reservoir. The spikes in sediment within the lakes formed by the Wheeler dam  
514 and Kentucky dam are due to large tributaries. The spike immediately after Fort Loudoun Dam  
515 (km 80) is also owing to a tributary confluence.



516

517 **Figure 6:** Longitudinal profile of sediment dynamics in the Catawba and Wateree and Tennessee Rivers.

518 Map of (a) Catawba and Wateree and (b) Tennessee Rivers with their dams. Trend in sediment

519 concentration and flux along the (c) Catawba and Wateree (d) Tennessee Rivers. The red dots show the

520 dam locations, whereas the blue and grey lines show the sediment concentration (mg/L) and adjusted

521 sediment flux (kg/s) obtained from the remote sensing data, respectively. The colored areas indicate the  
522 extent of reservoirs corresponding to the dams.

523

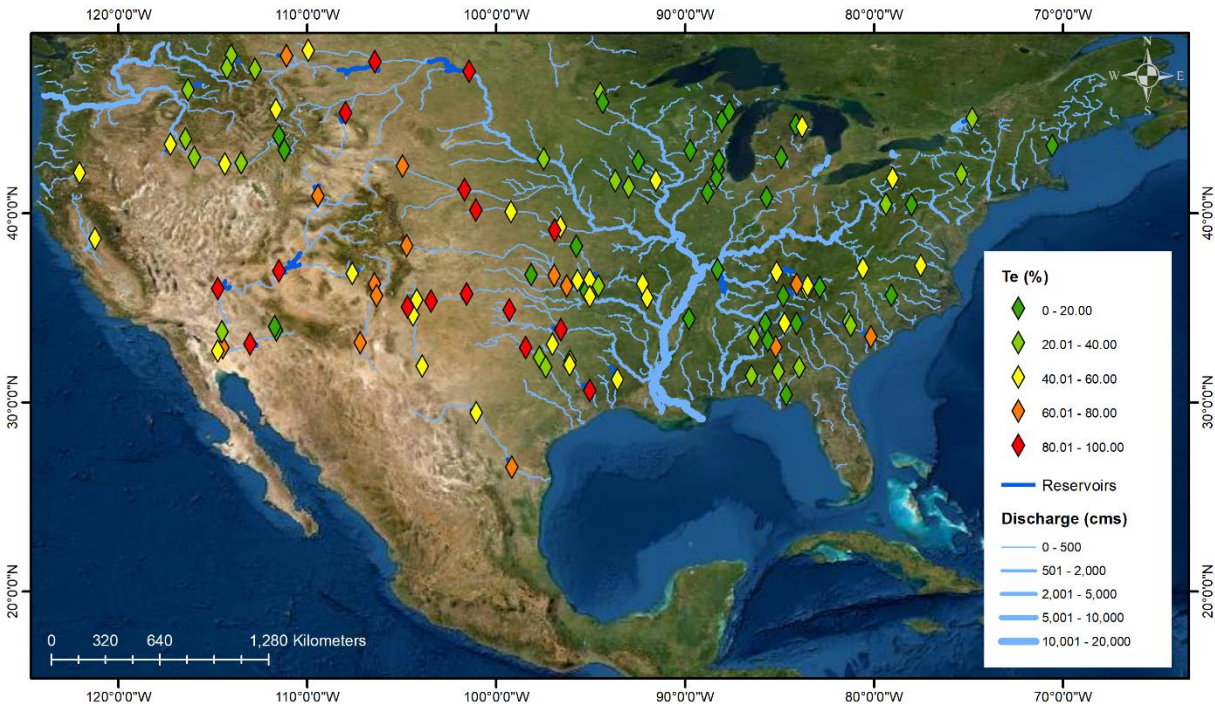
524 The longitudinal river sediment profiles constructed using the remote sensing data also reveal  
525 how the effect of trapping gradually decays downstream of dams. Increases (or replenishment) of  
526 sediment downstream of large dams can be attributed to several mechanisms: (1) increased  
527 transport capacity of the river flow, leading to channel scour, incision, and bank erosion  
528 (“hungry rivers”; Kondolf et al., 2014a; Kondolf et al., 2014b; Kummur et al., 2010), which was  
529 shown to rapidly increase sediment loads downstream (Brandt, 2000; Williams and Wolman,  
530 1984), (2) large tributaries that drain sediment into the main river, (3) eroded soil from the  
531 surrounding areas of the river reach catchment, and (4) dams may have mechanisms to release  
532 sediment downstream. The relative proportions of downstream sediment recovery that can be  
533 attributed to these processes need to be quantified to better understand downstream sediment  
534 recovery processes. However, this remains challenging mainly due to lack of data on sediment  
535 flows in most major tributaries, limiting our ability to calculate the mass balance of sediment  
536 along river corridors.

537

### 538 **3.3. Sediment Trapping Calculations for CONUS Dams**

539 Reservoir  $Te$  calculated using remote sensing-derived adjusted sediment flux values (Eq. 1) for  
540 the 116 dams, range from 0.3% to 98% with a mean of 43% and a standard deviation of 27.8%.  
541 Figure 7 shows the spatial variability of the remote sensing-calculated  $Te$ . It can be observed that  
542 dams with the largest  $Te$  values are mostly located in the arid mid-west regions of the US,  
543 whereas dams in the Eastern and North-West parts of the country generally have lower  $Te$   
544 values. This suggests that regional climate, particularly aridity, may be a factor that determines  
545  $Te$ , or serve as a proxy for a combination of properties that are common for dams in arid regions.  
546 These properties may include sediment particle size, reservoir size and depth, and dam  
547 operations. Many of the dams in the arid mid-west have large reservoirs, and limited or no ability  
548 to release sediment. Also, the sediments in this region tend to be coarser and are, therefore, more  
549 rapidly deposited due to higher settling velocity, once reaching the reservoir (Verstraeten and  
550 Poesen, 2000). Many of the dams on Eastern US rivers are not necessarily designed for storage  
551 (rather for navigation, hydropower generation etc.), and therefore, tend to be shallower and/or

552 can be run-of-river dams. Also, suspended sediments in these regions tend to be finer, which  
553 decreases their ability to be trapped. Vörösmarty et al. (2003) also found that dams in arid  
554 regions tend to have larger  $Te$  values due to their highly variable discharge regimes, high demand  
555 for water for irrigation and community water uses, and the resulting necessity to store water. The  
556 effect of the aridity index was further explored using Geographically Weighted Regression when  
557 developing the CONUS  $Te$  model, which is explained in section 3.4.  
558



559 **Figure 7:** Trapping efficiency ( $Te$ ; %) of the 116 dams calculated using observed remote sensing data.

560  
561 The rate of decreasing sediment flux (sedimentation) within individual reservoirs was calculated  
562 for all 116 dams using the amount of sediment trapped and the lake length along the longest part  
563 of the reservoir. The 116 reservoirs studied here have a mean trapping rate of 0.27 kg/s/km,  
564 ranging from 0.002 and 2.1 kg/s/km. The pattern of sediment decay within the reservoir length  
565 varies across reservoirs, but generally follows an exponential shape, with sedimentation rates  
566 decreasing along the reservoir downstream length (e.g., Figure 3b).

567

### 568 **3.4. CONUS $Te$ Model**

569 Twenty one (21) explanatory variables were tested to predict reservoir  $Te$  using machine learning  
570 methods as well as multiple linear regression, based on the  $Te$  derived for the 116 dams. The list  
571 of explanatory variables used is provided in Table 1.

572

573 A multiple regression model was developed after confirming that the data meet the necessary  
574 assumptions for regression. The model yielded an  $R^2$  of 0.68 (Adj.  $R^2 = 0.66$ ) using five  
575 variables: dam height (log converted), incoming sediment flux (log converted), outgoing water  
576 discharge (log converted), reservoir length along the longest part, and Aridity Index. All these  
577 variables significantly contribute to the regression model ( $p < 0.05$ ). This indicates that 68% of  
578 the variability in  $Te$  can be explained by these five variables with a Root Mean Square Error  
579 (RMSE) of 16.1% and a Nash Sutcliffe Efficiency (NSE) of 0.68. The resulting model equation  
580 is:

581

$$Te = 49.43 + 31.26 \log(Q_{s\_in}) - 37.05 \log(Q_{out}) + 19.68 \log(H) + 0.15 L - 13.81 AI \quad (2)$$

582

583 where  $Q_{s\_in}$  is the adjusted incoming sediment flux (kg/s),  $Q_{out}$  is the outgoing discharge (m<sup>3</sup>/s),  
584  $H$  is the dam height (m),  $L$  is the lake length along the longest part (km), and  $AI$  is the aridity  
585 index (higher values for humid regions) calculated for the reservoir polygon. The importance of  
586 the independent variables in the model in descending order based on the standard coefficients  
587 and contribution to change in the  $R^2$ , are  $Q_{out}$ ,  $Q_{s\_in}$ ,  $H$ ,  $L$ , and  $AI$ . Figure 8 shows the  
588 performance of the multiple linear regression model (Eq. 2) in predicting  $Te$ . Higher degree of  
589 scatter can be seen for low observed  $Te$ . Geographically Weighted Regression confirms a  
590 uniform distribution of Local  $R^2$ , and the maps of standard residual and standard error confirm a  
591 random distribution. This indicates a robust model and a consistent relationship between  
592 explanatory variables and observed  $Te$  in geographic space.

593  
594  
595  
596  
597  
598  
599  
600  
601  
602  
603  
604  
605  
606  
607  
608  
609  
610  
611  
612  
613  
614  
615  
616  
617  
618  
619  
620  
621  
622  
623

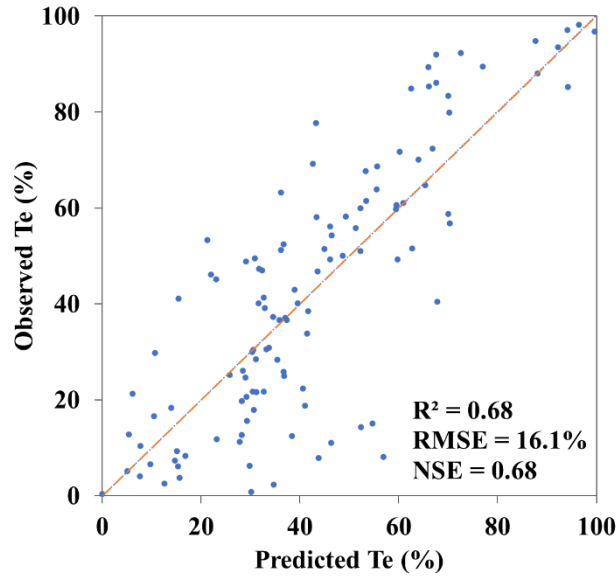
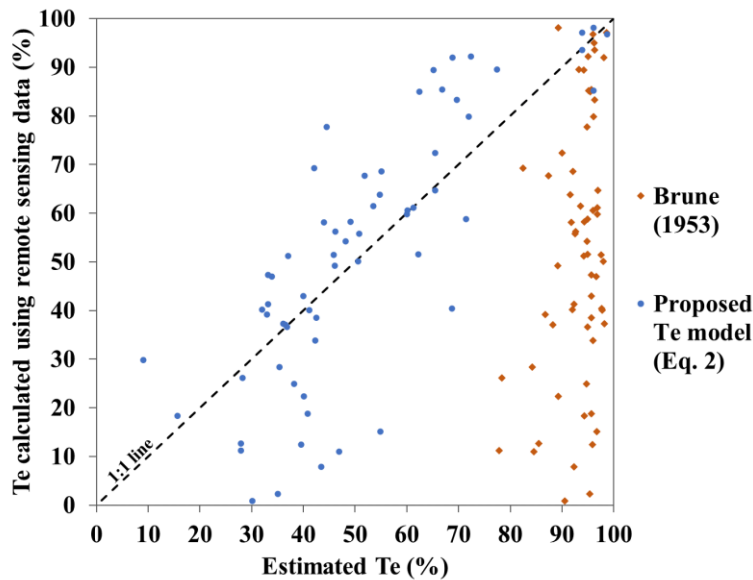


**Figure 8:** Evaluation of the  $T_e$  predicted by the regression model (Eq. 2) and the  $T_e$  calculated using remote sensing sediment data ( $n = 116$ ). The orange line is the 1:1 line. The trend line falls on the 1:1 line.

For comparison, we calculated  $T_e$  for these US dams using the Brune (1953) formula for individual reservoirs, later adopted globally by Vörösmarty et al. (2003) and Syvitski et al., (2005). This is currently the most widely used approach to represent sediment trapping in large-scale sediment transport models. This method predicts  $T_e$  for individual reservoirs as a function of local water residence time change, calculated as the effective reservoir capacity divided by local mean annual discharge. Figure 9 shows a comparison between  $T_e$  calculated using Eq. 2 and the Brune (1953) formula for reservoirs with  $> 0.5 \text{ km}^3$  storage capacity (defined as large reservoirs by Vörösmarty et al. (2003)). Our  $T_e$  model results in noticeably different values compared to the Brune (1953) approach. The most widely accepted idea about reservoir trapping efficiencies yielded by previous studies is that  $T_e$  is very large for large reservoirs and small for small reservoirs. Williams and Wolman (1984) suggested that  $T_e$  of large reservoirs are commonly greater than 99%. Vörösmarty et al. (2003) indicate that the  $T_e$  of large reservoirs is typically  $\sim 85\%$ . Contrary to these findings, our results show that reservoir volume (indicated by storage capacity) does not necessarily play an important role in determining sediment trapping. According to the remote sensing sediment data, large reservoirs can have a wide range of  $T_e$  values. This may be partly due to the fact that  $Q_{s,out}$  is capturing the downstream erosion to

624 some degree, leading to an underestimation of  $Te$ . The longitudinal profiles constructed using  
 625 remote sensing sediment data (section 3.2) show that the reduction in sediment is dramatic and  
 626 consistent downstream in some dams, while it is not the case in others. This consistency of  
 627 remote sensing SSC and flux downstream of the dams (for hundreds of km in some cases) is  
 628 evidence of the robustness of the data and the methodology in capturing the net effect of a dam.  
 629 Considering the possibility of under-predictions in  $Te$  due to erosion or remote sensing artifacts  
 630 downstream of a dam, our  $Te$  results and model may be considered as representing the net  
 631 reduction in sediment load due to damming (trapping – increase erosion). Capturing this net  
 632 effect is particularly important for sediment modeling studies to represent the actual effect of  
 633 dams and reservoirs in sediment trapping.



646 **Figure 9:** Comparison of  $Te$  calculated using the remote sensing data versus the proposed regression  
 647 model (blue) and Brune (1953) method (red), for reservoirs with  $>0.5 \text{ km}^3$  storage capacity ( $n=65$ ).  
 648

649 The model provides new insights into drivers of  $Te$ . The sediment flux entering the reservoir  
 650 plays an important role in governing trapping within the reservoir and  $Te$  is higher for higher  
 651 incoming sediment fluxes. A study that looked at reservoir trapping for individual storm events  
 652 found that, for similar detention times (length of time runoff from a storm event remains in the  
 653 reservoir), high incoming sediment loads had higher  $Te$  (Rausch and Heinemann, 1975). Rausch  
 654 and Schreiber (1981) also predicted  $Te$  for Callahan Reservoir by storm detention time, total

655 storm runoff, and mean inflow sediment concentration. One criticism that conventional methods  
656 such as Brune (1953) receive is that they are developed for normally ponded reservoirs mostly  
657 located in temperate settings and do not yield accurate results for tropical rivers with highly  
658 variable inflows, desilting, or semi-dry reservoirs (Lewis et al., 2013; Verstraeten and Poesen,  
659 2000). This may be because sediment trapping is highly influenced by the incoming sediment  
660 rates. The equations proposed here address this issue by incorporating sediment inflow to the  
661 reservoir as a predictor variable.

662

663 For lower rates of water discharge from the dam,  $Te$  is higher indicating less release of sediment  
664 and therefore, higher trapping values. The height of the dam is also included as a key variable  
665 indicating that taller or in general larger dams facilitate more trapping of sediment. Larger values  
666 of reservoir lengths provide sufficient time for sedimentation within the reservoir, leading to  
667 larger  $Te$  values. This parameter may be a proxy for sediment retention time of the reservoir  
668 which is widely used by methods such as Brune (1953) and Rausch and Heinemann (1975).  
669 Aridity index values obtained from Lin et al. (2020) which is originally based on Trabucco and  
670 Zomer (2019) indicates higher  $Te$  for dam impoundments in arid regions. This can also be clearly  
671 seen in the spatial distribution of  $Te$  shown in Figure 7. Further exploration of the influence of  
672 aridity on  $Te$  estimations using the Geographically Weighted Regression revealed that Aridity  
673 Index helps to minimize the regional spatial variability in  $Te$  estimates and makes the model  
674 geographically consistent.

675

676 In addition, the reservoir operating schemes and mechanisms, and timing of sediment release or  
677 flushing by the dam may act as important variables that govern  $Te$  (Brandt, 2000; Kondolf et al.,  
678 2014a). However, incorporating these aspects into  $Te$  calculations is difficult due to data  
679 limitations, difficulty in predicting the timing of these mechanisms, and complexity in  
680 incorporating it to trapping calculations. In this regard, the age of the dam as an explanatory  
681 variable may serve as a proxy, as newer dams tend to include sediment release mechanisms.  
682 However, dam age was found not to be a significant contributor to  $Te$  in this analysis.

683

684 Dam height, reservoir length parameters, and Aridity Index are widely available or can be  
685 extracted from existing datasets. Sediment fluxes into the reservoir and, in some cases, outgoing

686 discharge are more challenging to obtain. It may be possible in the future to measure outgoing  
687 discharge based on satellite approaches as well (Gleason and Durand, 2020), especially after the  
688 launch of the Surface Water and Ocean Topography (SWOT) mission (Biancamaria et al., 2016).  
689 To overcome the challenge of obtaining sediment data, a second model was developed using  
690 only widely available data to facilitate a wide range of applications:

$$691 \quad Te = -33.63 - 25.34 \log(Q_{out}) + 21.74 \log(H) + 19.08 \log(D) + 0.21 L \quad (3)$$

692 where  $D$  is drainage area (km<sup>2</sup>). Although this equation has a lower predictive accuracy  
693 compared to the previous equation ( $R^2=0.59$ ; Adj.  $R^2=0.57$ ; RMSE = 18.1%), it can provide  $Te$   
694 estimates for the US with reasonable accuracy for data-limited locations.

695  
696  
697 A machine learning model development was also attempted. In machine learning techniques,  
698 large datasets help to learn 'hidden' patterns from the data and therefore have the potential to  
699 achieve higher accuracies than simple statistical methods (Lin et al., 2020). However, machine  
700 learning techniques are generally suitable for large datasets. The best Random Forest model  
701 developed in this analysis yielded an  $R^2$  of 0.50 using all the explanatory variables with an  
702 RMSE of 19.72%. The Multi-Layer Perceptron model only achieved a predictive power of 0.22  
703 in terms of  $R^2$  with an RMSE of 24.64%. The relatively small training dataset available in this  
704 study likely hindered the development of a robust machine learning model.

### 705 706 **3.5. Global $Te$ Model**

707 We developed a third model for global-scale applications based on data from the commonly used  
708 Global Reservoir and Dam (GRanD) dataset (Lehner et al., 2011b). In addition to the remote  
709 sensing-derived  $Te$  of the 116 dams in the CONUS, 42 additional observed  $Te$  values outside the  
710 US were used to develop this model. The resulting model had an  $R^2=0.45$  (Adj.  $R^2=0.44$ ) and an  
711 RMSE of 22% using four explanatory variables:

$$712 \quad Te = -28.64 - 20.87 \log(Q_{out}) + 16.26 \log(D) + 24.17 \log(L) + 0.19 H \quad (4)$$

713

714 The Geographically Weighted Regression shows that this model is also consistent in geographic  
 715 space with a uniform distribution of Local  $R^2$ , and a random distribution of standard residuals  
 716 and standard error. Using this equation,  $Te$  was calculated for 6823 global dams in the GRanD  
 717 database for which data were available for essential explanatory variables, and dam  
 718 impoundments fall on the Grill et al. (2019) river network. For 70 GRanD dams that did not have  
 719 reservoir polygons (e.g., individual dams that do not form reservoirs), a zero  $Te$  was assigned to  
 720 indicate no sediment trapping for sediment modeling efforts. In addition, 54 dams primarily built  
 721 for navigation were also assigned a zero  $Te$ . The resulting global  $Te$  dataset (Figure 10) had an  
 722 average  $Te$  of 40.57% (Table 2).

723

724 **Table 2:** Descriptive statistics of  $Te$  values calculated using the global model.

	<b>Number of Reservoirs</b>	<b>Sum of reservoir capacities (km<sup>3</sup>)*</b>	<b>Mean <math>Te</math> (%)</b>	<b>Median <math>Te</math> (%)</b>	<b>Standard deviation <math>Te</math> (%)</b>
<b>Global</b>	<b>6823</b>	<b>6746 (1.0)</b>	<b>40.57</b>	<b>39.66</b>	<b>14.95</b>
Africa	624	1043.5 (1.67)	49.11	49.35	13.70
Asia	2203	2365.5 (1.07)	38.20	36.52	14.57
Australia and Oceania	234	95.5 (0.41)	42.68	43.76	14.97
Europe	1245	585.4 (0.47)	39.22	39.81	14.18
North America	2177	1734.5 (0.80)	42.14	39.35	15.40
South America	340	922 (2.7)	43.02	42.64	13.17

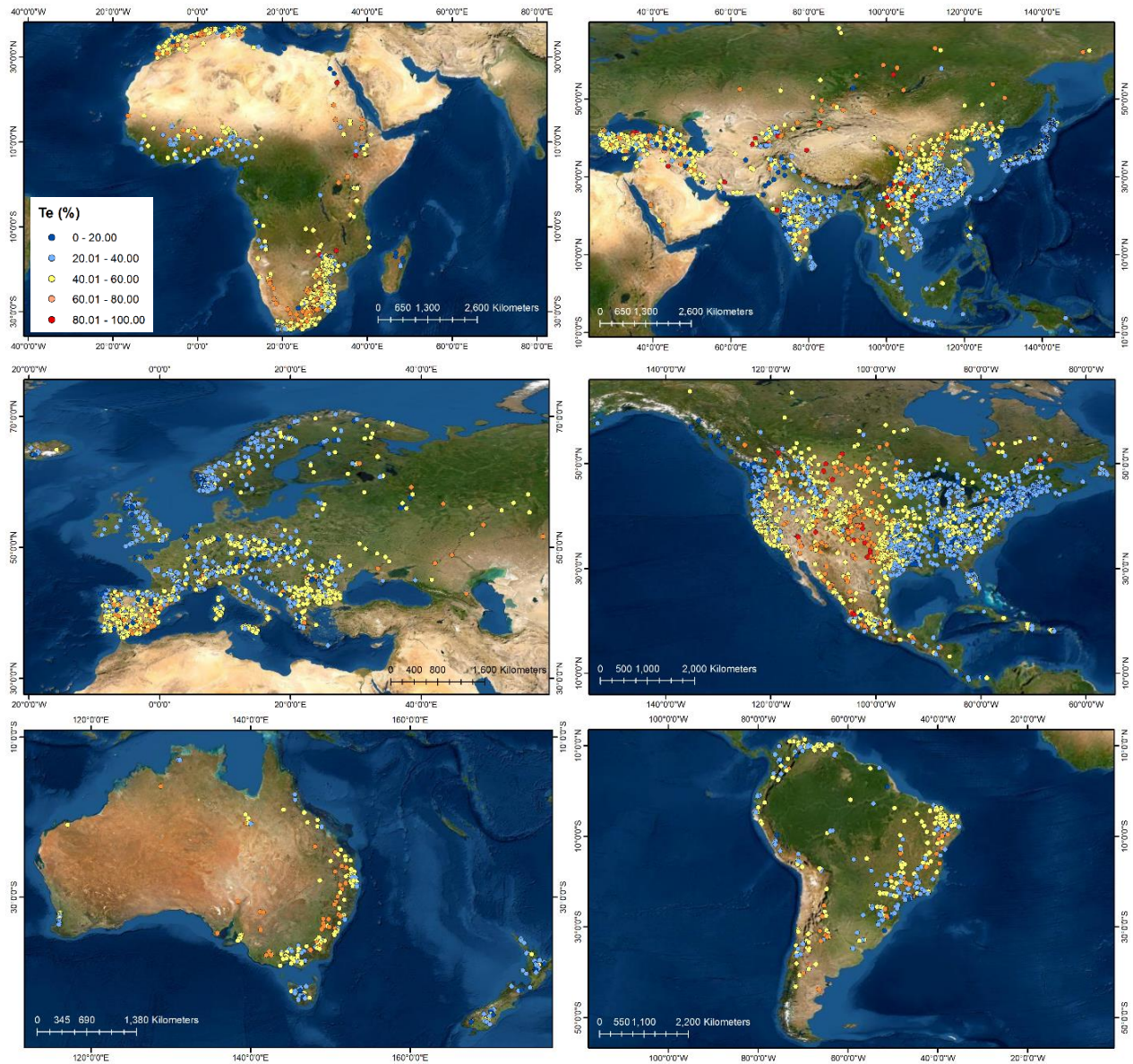
725 \*the number within parenthesis is the mean reservoir capacity

726

727 Continental-scale analysis (Table 2) shows that dams in Africa have the highest average  $Te$   
 728 (49.11%) in agreement with Vörösmarty et al. (2003) likely due to (i) a high proportion of dams  
 729 in arid regions, (ii) the resulting need to have large reservoir capacities to stabilize highly  
 730 variable river flows, and (iii) generally low river discharges (Vörösmarty et al., 2003). Asia  
 731 accounts for the largest number of dams in GRanD and the greatest sum of reservoir capacities  
 732 but has the lowest average  $Te$ . The reasons for this may include the location of dams in more  
 733 humid locations and rivers with high discharge. In addition, a large proportion of dams in humid  
 734 regions are hydropower dams with shorter water storage times and frequent water releases,  
 735 which can reduce their  $Te$ . The continent of North America, with the second highest number of  
 736 dams in GRanD and second highest cumulative reservoir capacity, has a relatively high average

737  $T_e$  as expected. However, these differences between continents in terms of average and median  
738  $T_e$  are small at this scale.

739



740

741 **Figure 10:** Global distribution of Reservoir  $T_e$  (%) calculated using equation 4 for 6823 dams in the  
742 GRanD dataset.

743

744 In order to test the regional dependency of  $T_e$ , we tested the explanatory variables to develop an  
745 equation only involving dam impoundments in China.  $T_e$  for dams in China can be predicted

746 with a high accuracy ( $R^2=0.80$ ; Adj.  $R^2=0.78$ ; RMSE = 11.25%) using only three variables; log  
747 drainage area, log reservoir surface area, and log reservoir capacity. The equation is as follows,  
748

$$Te = 230.44 - 43.3 \log(D) + 20.21 \log(S) + 29.24 \log(SA) \quad (5)$$

749  
750 where  $S$  is storage capacity of the reservoir ( $\text{km}^3$ ), and  $SA$  is reservoir surface area ( $\text{km}^2$ ). The  
751 negative relationship that upstream drainage area ( $D$ ) has with  $Te$  in this model can be explained  
752 by the negative relationship between  $Q$  and  $Te$  in the global model as well as the CONUS model.  
753 In regional settings,  $Q$  and  $D$  tend to have a strong correlation. This may also be indicative of the  
754 fact that large rivers with large drainage areas can have smaller  $Te$  values in this region.

755  
756 These different models for different regions indicate that  $Te$  may have a strong regional  
757 dependency and it may be more accurate to develop regional models (for regions smaller than  
758 continental scale) or calibrations for different settings. Some of the reasons for this regional  
759 dependency may include climate, river flow regimes, and dam type and operation. Our global  $Te$   
760 model has a relatively lower predictive capability compared to the CONUS  $Te$  model, largely  
761 due to data limitations. The remote sensing SSC dataset used here for the CONUS is currently in  
762 the process of being expanded globally. Once this product is available, observed  $Te$  can be  
763 calculated for global dams, allowing us to develop more robust empirical models for predicting  
764 global  $Te$  and potentially use machine learning techniques.

765

#### 766 **4. Conclusions**

767 As a major driver of anthropogenic disturbance of fluvial fluxes, the impact of damming on  
768 freshwater and coastal systems is key for reliably predicting modern and future sediment  
769 dynamics. Scarcity in sediment monitoring has limited the accuracy and universal applicability  
770 of sediment trapping parameterization in hydro-geomorphic models. Emerging remote sensing  
771 approaches now provide sediment concentration data at large spatial scales, offering unparalleled  
772 opportunities to improve our understanding of river sediment transport dynamics. Using such a  
773 dataset, we developed a new empirical model for calculating  $Te$  of US and global reservoirs,  
774 based on dam, riverine, and basin attributes. The simplicity of the models will allow modelers to  
775 easily incorporate them into their fluvial sediment models, potentially considerably improving

776 the models' ability to represent the effects of anthropogenic activities on sediment dynamics. We  
777 also argue that remote sensing-based  $Te$  calculations can be particularly useful for large-scale  
778 hydrological models to represent the trapping efficiencies of reservoirs more realistically than  
779 currently available methods derived using theoretical approaches, given that remote-sensing can  
780 capture the sediment flux downstream of the dams more accurately.

781  
782 In order to test how well remote sensing-captured surface sediment loads represent depth-  
783 averaged sediment loads of rivers, a comparison between USGS measured sediment fluxes and  
784 remote sensing-calculated sediment fluxes was conducted for 36 gaging stations. The results  
785 showed that, with an adjustment factor of 4.45, remote sensing-derived sediment strongly  
786 aligned with in-situ observations. In this study, we calculated  $Te$  for 116 individual dam  
787 impoundments across the US using remote sensing observations of long-term sediment data and  
788 used that to develop data-driven CONUS and global models to predict  $Te$ . When compared with  
789 the  $Te$  calculated by previous methods, remote sensing data reveal that large reservoirs can have  
790 a wide range of  $Te$  values, and reservoir volume (indicated by storage capacity) does not  
791 necessarily play an important role in determining sediment trapping. This is contrary to the  
792 previous claims that  $Te$  is very large for large reservoirs and small for small reservoirs.

793  
794 The development of regional and global models to predict  $Te$  revealed that regional models  
795 better predict  $Te$ , but global  $Te$  estimates are possible and can be used in global sediment  
796 transport modeling. We found that reservoir, climate, and fluvial sediment flux metrics are  
797 important controls of  $Te$  in both regional and global models. Moving forward,  $Te$  predictions  
798 could benefit from more site-specific and regional information (e.g., climate).

799  
800 Future work will include the implementation of the developed sediment trapping model within  
801 the WBMsed hydro-geomorphic modeling framework (Cohen et al., 2013, 2014). WBMsed is a  
802 spatially and temporally explicit global-scale model with a robust hydrological framework and  
803 well-established sediment modules. WBMsed  $Te$  module is currently based on the Vörösmarty et  
804 al. (2003) model. With forthcoming global remote sensing products of SSC,  $Te$  may also be  
805 dynamically assimilated directly for a large dataset of global dams. Improving the representation  
806 of sediment trapping in hydro-geomorphic models will aid in predicting current and future river

807 sediment transport, quantifying the global sediment delivery into the ocean, studying ecological  
808 impacts associated with sediment in freshwater systems, and understanding anthropogenic  
809 influences on riverine fluxes.

810

### 811 **Data Availability Statement**

812 The remote sensing river sediment dataset used for this study is available at  
813 <https://doi.org/10.5281/zenodo.4900563>.

814

### 815 **Acknowledgments**

816 This project was funded by a grant from the Alabama Water Institute (AWI; University of  
817 Alabama) Interdisciplinary Innovations Program. We thank Jida Wang for providing the  
818 encryption key to associate ICOLD dam attribute data with the GeoDAR database.

819

### 820 **References**

821 Best, J. and Darby, S.E. (2020). The Pace of Human-Induced Change in Large Rivers: Stresses,  
822 Resilience, and Vulnerability to Extreme Events. *One Earth*, 2(6), pp.510-514.

823 Best, J. (2019). Anthropogenic stresses on the world's big rivers. *Nature Geoscience*, 12(1),  
824 pp.7-21.

825 Biancamaria, S., Lettenmaier, D., & Pavelsky, T. (2016). The SWOT Mission and Its  
826 Capabilities for Land Hydrology. *Surveys in Geophysics*, 37(2), 307-337.

827 Biswas, A.K. and Tortajada, C. (2012). Impacts of the high Aswan Dam. In *Impacts of large*  
828 *dams: A global assessment* (pp. 379-395). Springer, Berlin, Heidelberg.

829 Blanchard, R.A., Ellison, C.A., Galloway, J.M., and Evans, D.A. (2011), Sediment  
830 concentrations, loads, and particle- size distributions in the Red River of the North and  
831 selected tributaries near Fargo, North Dakota, during the 2010 spring high-flow event: U.S.  
832 Geological Survey Scientific Investigations Report 2011–5064.

833 Borland, W.M. (1971). Reservoir sedimentation. In Shen, H.W., editor, *River mechanics*. Vol. II,  
834 Fort Collins, CO: Colorado State University, 29.1–29.38.

835

836 Brandt, S. A. (2000). Classification of geomorphological effects downstream of  
837 dams. *Catena*, 40(4), 375-401.

838

839 Brown, C.B. (1943). Discussion of Sedimentation in reservoirs, by J. Witzig. Proceedings of the  
840 American Society of Civil Engineers 69, 1493–1500.

841  
842 Brune, G.M. (1953). Trap efficiency of reservoirs. *Eos, Transactions American Geophysical*  
843 *Union*, 34(3), pp.407-418.

844 Chakrapani, G. J. (2005). Factors controlling variations in river sediment loads. *Current science*,  
845 569-575.

846  
847 Chen, C. (1975). Design of sediment retention basins. In *Proceedings, national symposium on*  
848 *urban hydrology and sediment control*, July, Lexington, KY: University of Kentucky, 285–  
849 98.

850  
851 Churchill, M.A. (1948). Discussion of Analyses and use of reservoir sedimentation data by L.C.  
852 Gottschalk. In *Proceedings of the federal inter- agency sedimentation conference*, Denver,  
853 Colorado, Washington, DC: US Geological Survey, 139–40.

854  
855 Cohen, S., Kettner, A.J., Syvitski, J.P. and Fekete, B.M. (2013). WBMsed, a distributed global-  
856 scale riverine sediment flux model: Model description and validation. *Computers &*  
857 *Geosciences*, 53, pp.80-93.

858  
859 Cohen, S., Kettner, A.J. and Syvitski, J.P. (2014). Global suspended sediment and water  
860 discharge dynamics between 1960 and 2010: Continental trends and intra-basin  
861 sensitivity. *global and planetary change*, 115, pp.44-58.

862  
863 Dethier, E.N., Renshaw, C.E. and Magilligan, F.J. (2020). Toward improved accuracy of remote  
864 sensing approaches for quantifying suspended sediment: Implications for suspended-  
865 sediment monitoring. *Journal of Geophysical Research: Earth Surface*, 125(7),  
866 p.e2019JF005033.

867  
868 Dunn, F.E., Darby, S.E., Nicholls, R.J., Cohen, S., Zarfl, C. and Fekete, B.M. (2019). Projections  
869 of declining fluvial sediment delivery to major deltas worldwide in response to climate  
870 change and anthropogenic stress. *Environmental Research Letters*, 14(8), p.084034.

871  
872 Espinosa-Villegas, C. O., & Schnoor, J. L. (2009). Comparison of long-term observed sediment  
873 trap efficiency with empirical equations for Coralville Reservoir, Iowa. *Journal of*  
874 *Environmental Engineering*, 135(7), 518-525.

875  
876 ESRI, (2021). USA Detailed Water Bodies layer package for ArcGIS (downloaded from  
877 <https://www.arcgis.com/home/item.html?id=84e780692f644e2d93cefc80ae1eba3a>)  
878

879 Fagundes, H.O, de Paiva, R.C.D., Fan, F.M., Buarque, D.C. and Fassoni-Andrade, A.C. (2020).  
880 Sediment modeling of a large-scale basin supported by remote sensing and in-situ  
881 observations. *Catena*, 190, p.104535.

882  
883 Gardner, J. R., Yang, X., Topp, S. N., Ross, M. R. V., Altenau, E. H., & Pavelsky, T. M. (2021).  
884 The color of rivers. *Geophysical Research Letters*, 48, e2020GL088946. [https://doi.](https://doi.org/10.1029/2020GL088946)  
885 [org/10.1029/2020GL088946](https://doi.org/10.1029/2020GL088946).

- 886 Gardner, J., Pavelsky, T., Yang, X., Topp, S., & Ross, M. (2022). River Sediment Database  
887 (RiverSed) (v1.0.0) [Data set]. Zenodo. <https://doi.org/10.5281/zenodo.4900563>
- 888 Gleason, C. J., & Durand, M. T. (2020). Remote sensing of river discharge: a review and a  
889 framing for the discipline. *Remote Sensing*, 12(7), 1107.
- 890 Grill, G., Lehner, B., Thieme, M., Geenen, B., Tickner, D., Antonelli, F., Babu, S., Borrelli, P.,  
891 Cheng, L., Crochetiere, H. and Macedo, H.E. (2019). Mapping the world's free-flowing  
892 rivers. *Nature*, 569(7755), pp.215-221.
- 893 Haddeland, I., Heinke, J., Biemans, H., Eisner, S., Flörke, M., Hanasaki, N., Konzmann, M.,  
894 Ludwig, F., Masaki, Y., Schewe, J. and Stacke, T. (2014). Global water resources affected by  
895 human interventions and climate change. *Proceedings of the National Academy of*  
896 *Sciences*, 111(9), pp.3251-3256.
- 897 Heinemann, H.G. (1984). Reservoir trap efficiency. In Hadley, R.F. and Walling, D.E., editors,  
898 *Erosion and sediment yield: some methods of measurement and modelling*, Norwich:  
899 *GeoBooks*, 201–18.  
900
- 901 Hu, B., Yang, Z., Wang, H., Sun, X., Bi, N. and Li, G. (2009). Sedimentation in the Three  
902 Gorges Dam and the future trend of Changjiang (Yangtze River) sediment flux to the  
903 sea. *Hydrology and Earth System Sciences*, 13(11), pp.2253-2264.  
904
- 905 Jothiprakash, V. and Vaibhav, G.A.R.G. (2008). Re-look to conventional techniques for trapping  
906 efficiency estimation of a reservoir. *International Journal of Sediment Research*, 23(1),  
907 pp.76-84.  
908
- 909 Kondolf, G.M., Gao, Y., Annandale, G.W., Morris, G.L., Jiang, E., Zhang, J., Cao, Y., Carling,  
910 P., Fu, K., Guo, Q. and Hotchkiss, R. (2014a). Sustainable sediment management in  
911 reservoirs and regulated rivers: Experiences from five continents. *Earth's Future*, 2(5),  
912 pp.256-280.
- 913 Kondolf, G.M., Rubin, Z.K. and Minear, J.T. (2014b). Dams on the Mekong: Cumulative  
914 sediment starvation. *Water Resources Research*, 50(6), pp.5158-5169.  
915
- 916 Kumm, M., Lu, X. X., Wang, J. J., & Varis, O. (2010). Basin-wide sediment trapping efficiency  
917 of emerging reservoirs along the Mekong. *Geomorphology*, 119(3-4), 181-197.  
918
- 919 Laguionie, P., Crave, A. and Jigorel, A. (2007). Velocity and suspended sediment concentration  
920 profiles in rivers: in situ measurements and flux modelling. *WIT Transactions on Ecology*  
921 *and the Environment*, 104, pp.335-343.  
922
- 923 Latrubesse, E.M., Arima, E.Y., Dunne, T., Park, E., Baker, V.R., d'Horta, F.M., Wight, C.,  
924 Wittmann, F., Zuanon, J., Baker, P.A. and Ribas, C.C. (2017). Damming the rivers of the  
925 Amazon basin. *Nature*, 546(7658), pp.363-369.

- 926 Lehner, B., Liermann, C.R., Revenga, C., Vörösmarty, C., Fekete, B., Crouzet, P., Döll, P.,  
 927 Endejan, M., Frenken, K., Magome, J. and Nilsson, C. (2011a). High-resolution mapping of  
 928 the world's reservoirs and dams for sustainable river-flow management. *Frontiers in Ecology  
 929 and the Environment*, 9(9), pp.494-502.
- 930 Lehner, B., Liermann, C.R., Revenga, C., Vörösmarty, C., Fekete, B., Crouzet, P., Döll, P.,  
 931 Endejan, M., Frenken, K., Magome, J. and Nilsson, C. (2011b). Global reservoir and dam  
 932 (grand) database. *Technical Documentation, Version, 1*, pp.1-14.
- 933 Lewis, S.E., Bainbridge, Z.T., Kuhnert, P.M., Sherman, B.S., Henderson, B., Dougall, C.,  
 934 Cooper, M. and Brodie, J.E. (2013). Calculating sediment trapping efficiencies for reservoirs  
 935 in tropical settings: a case study from the Burdekin Falls Dam, NE Australia. *Water  
 936 Resources Research*, 49(2), pp.1017-1029.
- 937 Li, L., Ni, J., Chang, F., Yue, Y., Frolova, N., Magritsky, D., Borthwick, A.G., Ciais, P., Wang,  
 938 Y., Zheng, C. and Walling, D.E. (2020). Global trends in water and sediment fluxes of the  
 939 world's large rivers. *Science Bulletin*, 65(1), pp.62-69.
- 940 Lin, P., Pan, M., Allen, G.H., de Frasson, R.P., Zeng, Z., Yamazaki, D. and Wood, E.F. (2020).  
 941 Global estimates of reach-level bankfull river width leveraging big data geospatial  
 942 analysis. *Geophysical Research Letters*, 47(7), p.e2019GL086405.
- 943 Lu, X.X., Ran, L.S., Liu, S., Jiang, T., Zhang, S.R. and Wang, J.J. (2013). Sediment loads  
 944 response to climate change: A preliminary study of eight large Chinese rivers. *International  
 945 Journal of Sediment Research*, 28(1), pp.1-14.
- 946 McKay, L., Bondelid, T., Dewald, T., Rea, A., Johnston, C. and Moore, R. (2015). NHDPlus  
 947 version 2: user guide (data model version 2.1). *Horizon Systems*.
- 948 Merritt, W.S., Letcher, R.A. and Jakeman, A.J. (2003). A review of erosion and sediment  
 949 transport models. *Environmental modelling & software*, 18(8-9), pp.761-799.
- 950 Moore, R.B., McKay, L.D., Rea, A.H., Bondelid, T.R., Price, C.V., Dewald, T.G., and Johnston,  
 951 C.M. (2019). User's guide for the national hydrography dataset plus (NHDPlus) high  
 952 resolution: U.S. Geological Survey Open-File Report 2019– 1096, 66 p.,  
 953 <https://doi.org/10.3133/ofr20191096>.
- 954 Mulligan, M., van Soesbergen, A. and Sáenz, L. (2020). GOODD, a global dataset of more than  
 955 38,000 georeferenced dams. *Scientific Data*, 7(1), pp.1-8.
- 956 Narayanan, A. (2022). Sediment Response to Deforestation in the Amazon River Basin. Master's  
 957 Thesis, University of Alabama, USA.
- 958 Overeem, I., Hudson, B.D., Syvitski, J.P., Mikkelsen, A.B., Hasholt, B., Van Den Broeke, M.R.,  
 959 Noël, B.P.Y. and Morlighem, M. (2017). Substantial export of suspended sediment to the  
 960 global oceans from glacial erosion in Greenland. *Nature Geoscience*, 10(11), pp.859-863.

- 961 Pelletier, J.D. (2012). A spatially distributed model for the long-term suspended sediment  
 962 discharge and delivery ratio of drainage basins. *Journal of Geophysical Research: Earth*  
 963 *Surface*, 117(F2).
- 964 Rausch, D.L. and Heinemann, H.G. (1975). Controlling reservoir trap efficiency. *Transactions of*  
 965 *the ASAE*, 18(6), pp.1105-1108.
- 966 Rausch, D.L. and Schreiber, J.D. (1981). *Sediment and nutrient trap efficiency of a small flood-*  
 967 *detention reservoir* (Vol. 10, No. 3, pp. 288-293). American Society of Agronomy, Crop  
 968 Science Society of America, and Soil Science Society of America.
- 969  
 970  
 971  
 972 Rodgers, K.D. (2017). A Reservoir Morphology Database for the Conterminous United States:  
 973 U.S. Geological Survey data release, <https://doi.org/10.5066/F7GF0RQZ>
- 974 Schmidt, J.C. and Wilcock, P.R. (2008). Metrics for assessing the downstream effects of  
 975 dams. *Water Resources Research*, 44(4).
- 976 Sharma, D.K., Sharma, S.K. and Suri, S. (2018). Sediment Management of Projects on  
 977 Himalayan Rivers-A Case Study of Bhakra Dam and Beas Sutlej Link Project. *INCOLD*  
 978 *Journal (A Half Yearly Technical Journal of Indian Committee on Large Dams)*, 7(2), pp.3-  
 979 8.  
 980  
 981
- 982 Syvitski, J. P. (2003). Supply and flux of sediment along hydrological pathways: research for the  
 983 21st century. *Global and Planetary Change*, 39(1-2), 1-11.
- 984 Syvitski, J. P., Vörösmarty, C. J., Kettner, A. J., & Green, P. (2005). Impact of humans on the  
 985 flux of terrestrial sediment to the global coastal ocean. *science*, 308(5720), 376-380.
- 986  
 987 Syvitski, J., Ángel, J. R., Saito, Y., Overeem, I., Vörösmarty, C. J., Wang, H., & Olago, D.  
 988 (2022). Earth's sediment cycle during the Anthropocene. *Nature Reviews Earth &*  
 989 *Environment*, 3(3), 179-196.
- 990  
 991 Syvitski, J.P. and Kettner, A. (2011). Sediment flux and the Anthropocene. *Philosophical*  
 992 *Transactions of the Royal Society A: Mathematical, Physical and Engineering*  
 993 *Sciences*, 369(1938), pp.957-975.
- 994  
 995 Syvitski, J.P., Milliman, J.D. (2007). Geology, geography, and humans battle for dominance over  
 996 the delivery of fluvial sediment to the coastal ocean. *J. Geol.*115 (1), pp.1–19.
- 997 Tan, G., Chen, P., Deng, J., Xu, Q., Tang, R., Feng, Z., & Yi, R. (2019). Review and  
 998 improvement of conventional models for reservoir sediment trapping  
 999 efficiency. *Heliyon*, 5(9), e02458.
- 1000  
 1001 USDA-SCS, (1983). National engineering hand- book (2nd edn) (Section 3: 'Sedimentation';  
 1002 Chapter 8 'Sediment storage design criteria') Washington, DC: US Department of  
 1003 Agriculture.

1004  
1005 Trabucco, A. and Zomer, R.J. (2019). Global aridity index and potential evapotranspiration  
1006 (ET0) climate database v2. *CGIAR Consort Spat Inf*, 10, p.m9.  
1007

1008 Vercruyssen, K., Grabowski, R.C. and Rickson, R.J. (2017). Suspended sediment transport  
1009 dynamics in rivers: Multi-scale drivers of temporal variation. *Earth-Science Reviews*, 166,  
1010 pp.38-52.  
1011

1012 Verstraeten, G. and Poesen, J. (2000). Estimating trap efficiency of small reservoirs and ponds:  
1013 methods and implications for the assessment of sediment yield. *Progress in Physical*  
1014 *Geography*, 24(2), pp.219-251.  
1015

1016 Vörösmarty, C.J., Meybeck, M., Fekete, B., Sharma, K., Green, P., Syvitski, J.P.M. (2003).  
1017 Anthropogenic sediment retention: major global impact from registered river impoundments.  
1018 *Glob. Planet. Chang.* 39 (1-2), pp.169-190.

1019 Wada, Y., de Graaf, I.E. and van Beek, L.P. (2016). High-resolution modeling of human and  
1020 climate impacts on global water resources. *Journal of Advances in Modeling Earth*  
1021 *Systems*, 8(2), pp.735-763.

1022 Walling, D.E. (2012). The role of dams in the global sediment budget. *IAHS-AISH publication*,  
1023 pp.3-11.  
1024

1025 Wang, K., Gelda, R.K., Mukundan, R. and Steinschneider, S. (2021a). Inter-model Comparison  
1026 of Turbidity-Discharge Rating Curves and the Implications for Reservoir Operations  
1027 Management. *JAWRA Journal of the American Water Resources Association*, 57(3), pp.430-  
1028 448.  
1029

1030 Wang, J., Walter, B.A., Yao, F., Song, C., Ding, M., Maroof, A.S., Zhu, J., Fan, C., Xin, A.,  
1031 McAlister, J.M. and Sikder, S. (2021b). GeoDAR: Georeferenced global dam and reservoir  
1032 dataset for bridging attributes and geolocations. *Earth System Science Data Discussions*,  
1033 pp.1-52.  
1034

1035 Wei, X., Sauvage, S., Ouillon, S., Le, T. P. Q., Orange, D., Herrmann, M., & Sanchez-Perez, J.  
1036 M. (2021). A modelling-based assessment of suspended sediment transport related to new  
1037 damming in the Red River basin from 2000 to 2013. *Catena*, 197, 104958.  
1038

1039 Wohl, E. and Rathburn, S. (2003). Mitigation of sedimentation hazards downstream from  
1040 reservoirs. *International Journal of Sediment Research*, 18(2), pp.97-106.  
1041

1042 Williams, G.P. and Wolman, M.G. (1984). *Downstream effects of dams on alluvial rivers* (Vol.  
1043 1286). US Government Printing Office.  
1044

1045 Wu, Z., Zhao, D., Syvitski, J.P., Saito, Y., Zhou, J. and Wang, M. (2020). Anthropogenic  
1046 impacts on the decreasing sediment loads of nine major rivers in China, 1954–2015. *Science*  
1047 *of the Total Environment*, 739, p.139653.

1048 Yang, X., Pavelsky, T.M., Ross, M.R., Januchowski-Hartley, S.R., Dolan, W., Altenau, E.H.,  
1049 Belanger, M., Byron, D., Durand, M., Van Dusen, I. and Galit, H. (2022). Mapping flow-  
1050 obstructing structures on global rivers. *Water Resources Research*, 58(1),  
1051 p.e2021WR030386.

1052 Zarfl, C., Lumsdon, A.E., Berlekamp, J., Tydecks, L., and Tockner, K. (2015). A global boom in  
1053 hydropower dam construction. *Aquat. Sci.* 77, 161–171, [https://doi.org/10.1007/s00027-014-](https://doi.org/10.1007/s00027-014-0377-0)  
1054 [0377-0](https://doi.org/10.1007/s00027-014-0377-0).

1055 **Supplementary materials**

1056

1057 **Table S1:** USGS gage observations (O-) used for validation of suspended sediment flux (Qs) and  
1058 discharge (Q)

ID	USGS site #	Lat	Lon	Area (km <sup>2</sup> )	USGS O-Qs time period	USGS O-Qs (kg/s)	USGS O-Q (m <sup>3</sup> /s)	Remote sensing Qs (kg/s)	NHDplus Q (m <sup>3</sup> /s)
1	01357500	42.79	-73.71	8,935	2003-2018	15.05	179.84	3.99	171.91
2	06486000	42.49	-96.41	814,811	1992-2019	257.31	909.59	40.53	1066.60
3	06610000	41.26	-95.92	836,049	1992-2019	476.65	1056.64	65.95	1065.09
4	06807000	40.68	-95.85	1,061,896	1992-2019	736.73	1259.21	118.54	1262.72
5	01331095	42.94	-73.65	9,772	1992-2001	2.61	198.59	2.05	183.99
6	05587455	38.95	-90.37	443,665	1990-2016	690.98	3665.79	204.44	3681.30
7	12340500	46.88	-113.93	15,594	1989-2016	3.65	79.48	1.14	83.65
8	07020500	37.90	-89.83	1,835,267	1988-2016	2659.89	6810.37	638.16	6483.72
9	04193500	41.50	-83.71	16,395	1988-2003	36.70	171.62	11.46	157.98
10	02489500	30.79	-89.82	17,024	1986-1993	39.20	284.70	15.35	330.61
11	05474000	40.75	-91.28	11,168	1985-2019	64.06	100.35	7.37	90.94
12	06452000	43.75	-99.56	25,680	1985-2019	111.70	21.61	3.08	17.83
13	05465500	41.18	-91.18	32,375	1985-2019	74.09	313.70	12.19	282.50
14	11303500	37.68	-121.27	35,066	1985-2019	7.79	108.86	3.68	134.60
15	08330000	35.09	-106.68	45,169	1985-2019	28.16	33.52	7.76	39.21
16	08332010	34.42	-106.80	49,806	1985-2019	24.67	28.87	5.86	27.66
17	08354900	34.26	-106.89	69,334	1985-2019	81.17	29.15	5.99	26.07
18	08358400	33.68	-107.00	71,743	1985-2019	71.14	22.33	9.30	24.72
19	11447650	38.46	-121.50	nan	1985-2019	41.72	587.21	15.39	749.23
20	05325000	44.17	-94.00	38,591	1985-2017	46.22	186.17	5.35	141.84
21	07010000	38.63	-90.18	1,805,223	1985-2017	2642.23	6522.81	572.56	6194.66
22	07022000	37.22	-89.46	1,847,181	1985-2017	2557.32	7081.22	658.07	6699.36
23	05586100	39.70	-90.65	69,264	1985-2011	170.20	740.62	39.04	722.86
24	05481650	41.68	-93.67	15,128	1985-2004	5.63	114.59	2.24	110.19
25	04198000	41.31	-83.16	3,240	1985-2002	7.62	36.61	2.44	33.25
26	05288500	45.13	-93.30	49,469	1985-1996	7.84	284.49	4.21	272.13
27	02116500	35.86	-80.39	5,905	1985-1994	20.40	82.78	4.81	91.75
28	09364500	36.72	-108.20	3,522	1985-1993	13.19	22.66	1.63	25.67
29	09217000	41.52	-109.45	36,260	1985-1992	3.16	41.63	1.28	53.22
30	01638500	39.27	-77.54	24,996	1985-1991	35.13	286.29	7.15	301.42
31	06115200	47.63	-108.69	105,281	1985-1991	138.49	231.88	23.02	268.70
32	06329500	47.68	-104.16	178,966	1985-1991	206.37	320.78	54.76	353.50

33	01567000	40.48	-77.13	8,687	1985-1990	2.83	127.17	2.63	130.88
34	05454500	41.66	-91.54	8,472	1985-1987	8.45	79.30	2.06	71.13
35	09368000	36.78	-108.68	33,411	1985-1986	108.66	47.48	4.61	61.73
36	12334550	46.83	-113.81	9,472	1986-2016	1.61	37.22	0.85	40.15

1059

1 **Supplementary materials**

2

3 **Table S1:** USGS gage observations (O-) used for validation of suspended sediment flux (Qs) and  
 4 discharge (Q)

ID	USGS site #	Lat	Lon	Area (km <sup>2</sup> )	USGS O-Qs time period	USGS O-Qs (kg/s)	USGS O-Q (m <sup>3</sup> /s)	Remote sensing Qs (kg/s)	NHDplus Q (m <sup>3</sup> /s)
1	01357500	42.79	-73.71	8,935	2003-2018	15.05	179.84	3.99	171.91
2	06486000	42.49	-96.41	814,811	1992-2019	257.31	909.59	40.53	1066.60
3	06610000	41.26	-95.92	836,049	1992-2019	476.65	1056.64	65.95	1065.09
4	06807000	40.68	-95.85	1,061,896	1992-2019	736.73	1259.21	118.54	1262.72
5	01331095	42.94	-73.65	9,772	1992-2001	2.61	198.59	2.05	183.99
6	05587455	38.95	-90.37	443,665	1990-2016	690.98	3665.79	204.44	3681.30
7	12340500	46.88	-113.93	15,594	1989-2016	3.65	79.48	1.14	83.65
8	07020500	37.90	-89.83	1,835,267	1988-2016	2659.89	6810.37	638.16	6483.72
9	04193500	41.50	-83.71	16,395	1988-2003	36.70	171.62	11.46	157.98
10	02489500	30.79	-89.82	17,024	1986-1993	39.20	284.70	15.35	330.61
11	05474000	40.75	-91.28	11,168	1985-2019	64.06	100.35	7.37	90.94
12	06452000	43.75	-99.56	25,680	1985-2019	111.70	21.61	3.08	17.83
13	05465500	41.18	-91.18	32,375	1985-2019	74.09	313.70	12.19	282.50
14	11303500	37.68	-121.27	35,066	1985-2019	7.79	108.86	3.68	134.60
15	08330000	35.09	-106.68	45,169	1985-2019	28.16	33.52	7.76	39.21
16	08332010	34.42	-106.80	49,806	1985-2019	24.67	28.87	5.86	27.66
17	08354900	34.26	-106.89	69,334	1985-2019	81.17	29.15	5.99	26.07
18	08358400	33.68	-107.00	71,743	1985-2019	71.14	22.33	9.30	24.72
19	11447650	38.46	-121.50	nan	1985-2019	41.72	587.21	15.39	749.23
20	05325000	44.17	-94.00	38,591	1985-2017	46.22	186.17	5.35	141.84
21	07010000	38.63	-90.18	1,805,223	1985-2017	2642.23	6522.81	572.56	6194.66
22	07022000	37.22	-89.46	1,847,181	1985-2017	2557.32	7081.22	658.07	6699.36
23	05586100	39.70	-90.65	69,264	1985-2011	170.20	740.62	39.04	722.86
24	05481650	41.68	-93.67	15,128	1985-2004	5.63	114.59	2.24	110.19
25	04198000	41.31	-83.16	3,240	1985-2002	7.62	36.61	2.44	33.25
26	05288500	45.13	-93.30	49,469	1985-1996	7.84	284.49	4.21	272.13
27	02116500	35.86	-80.39	5,905	1985-1994	20.40	82.78	4.81	91.75
28	09364500	36.72	-108.20	3,522	1985-1993	13.19	22.66	1.63	25.67
29	09217000	41.52	-109.45	36,260	1985-1992	3.16	41.63	1.28	53.22
30	01638500	39.27	-77.54	24,996	1985-1991	35.13	286.29	7.15	301.42
31	06115200	47.63	-108.69	105,281	1985-1991	138.49	231.88	23.02	268.70
32	06329500	47.68	-104.16	178,966	1985-1991	206.37	320.78	54.76	353.50

33	01567000	40.48	-77.13	8,687	1985-1990	2.83	127.17	2.63	130.88
34	05454500	41.66	-91.54	8,472	1985-1987	8.45	79.30	2.06	71.13
35	09368000	36.78	-108.68	33,411	1985-1986	108.66	47.48	4.61	61.73
36	12334550	46.83	-113.81	9,472	1986-2016	1.61	37.22	0.85	40.15

5